Iraqi National Journal of Earth Science
www.earth.uomosul.edu.iq

Mineralogy and Geochemistry of Upper Cretaceous and Paleogene Succession in Gali and Qalbaza Sections, Northeastern Iraq: Implications for Provenance and Detecting K/Pg Boundary

Shareef T. Al-Hamed [1*], **Sattar J. Al-Khafaji** [2]

[1] *Department of Geology and Petroleum, College of Science, University of Mosul, Mosul, Iraq.*
[2] *Department of Geology, College of Science, University of Basrah, Basrah, Iraq.*

Article information

Received: 01- Nov -2024
Revised: 28- Nov -2024
Accepted: 18- Dec -2024
Available online: 01- Jan -2026

Keywords:
Geochemistry,
Tanjero/Kolosh,
K/Pg boundary,
Cretaceous,
Paleogene,

Correspondence:
Name: Shareef T. Al-Hamed
Email: shareefalhamed82@gmail.com

ABSTRACT

One of the most controversial topics in geology is the K/Pg event, marked by mineralogical and geochemical evidence, as well as environmental catastrophes that led to a massive extinction. At the end of the Mesozoic, the Chicxulub meteorite impact and/or prolonged Deccan eruptions were the causes of the global mineralogical and geochemical anomalies at the K/Pg. The Gali and Qalbaza sections in Iraq represent the K/Pg between the upper Tanjero and lower Kolosh formations. The sandstones of these sections are immature lithic graywacke derived from an undissected arc-recycled orogenic provenance, and they were deposited in an arid to semi-arid paleoclimate. REE suggests that a single melt underwent differentiation to provide the source rocks that weathered and were deposited under oxic-anoxic paleoredox conditions. Quartz and K-feldspar increase and carbonate fragments decrease at 10 cm thick of both gray siltstone (sample G19 of Gali section) and red conglomerate layers (sample Q18 of Qalbaza section). The G19 and Q18 layers exhibit low calcite content and the presence of analcime, smectite, and vermiculite. Positive anomalies for SiO_2, Al_2O_3, Fe_2O_3, MgO, Na_2O, K_2O, TTEs, Zr, Zn, and Cu, and negative anomalies for CaO, MnO, LOI, Hf, Sr, and Cs are recorded at 10 cm thick G19 and Q18 layers. Elevated levels of Fe/Al, Ni/Al, Cr/Al, and SO_2/MnO are also detected at the G19 and Q18 layers. Based on the current evidence, the proposed boundaries of gray siltstone (sample G19) and red conglomerate (sample Q18) layers could represent the K/Pg boundaries, with parts of them perhaps eroded.

DOI: 10.33899/injes.v26i1.60186, ©Authors, 2026, College of Science, University of Mosul.

معدنية وجيوكيميائية تتابعات الكريتاسي الاعلى والباليوجين في مقطعي كَلي وكالبازا، شمال شرقي العراق: يتضمن الاصل وتحديد حد الكريتاسي/الباليوجين

شريف ثمود الحامد[1]* ، ستار جبار الخفاجي [2]

[1] قسم علم الارض والنفط، كلية العلوم، جامعة الموصل، الموصل، العراق.

[2] قسم علم الارض، كلية العلوم، جامعة البصرة، البصرة، العراق.

معلومات الارشفة

تاريخ الاستلام: 01- نوفمبر - 2024

تاريخ المراجعة: 28- نوفمبر - 2024

تاريخ القبول: 18- ديسمبر - 2024

تاريخ النشر الالكتروني: 01- يناير - 2026

الكلمات المفتاحية:
جيوكيميائية،
تانجيرو/كولوش،
حدود K/Pg،
كريتاسي،
باليوجين،

المراسلة:

الاسم: شريف ثمود الحامد

Email: shareefalhamed82@gmail.com

الملخص

يُعد حدث K/Pg وهو حد الكريتاسي/الباليوجين من أكثر المواضيع المثيرة للجدل في علم الأرض، والذي يتميز بأدلةٍ معدنية وجيوكيميائية وكوارث بيئية سببت انقراضاً جماعياً. ان اصطدام نيزك جيكسولوب و/او دفقات براكين ديكان طويلة الامد في نهاية الحقبة المتوسطة (Mesozoic) هي الاحداث التي تقف وراء الشذوذات المعدنية والجيوكيميائية العالمية عند حد K/Pg. يمثل مقطعا كَلي وكالبازا في العراق حد K/Pg بين تكويني تانجيرو الاعلى وكولوش الاسفل. الصخور الرملية لهذه المقاطع عبارة عن (lithic graywacke) غير ناضجة مشتقة من أصل اوروجيني قوسي معاد الترسيب، وقد ترسبت في مناخ قديم جاف الى شبه جاف. تُشير العناصر الأرضية النادرة إلى أن صهيراً مفرداً عانى من التفاضل لتوفير الصخور المصدرية التي تجوت وترسبت تحت ظروف مؤكسدة – مختزلة. يزداد المرو والفلدسبار البوتاسي وتنخفض القطع الكاربوناتية عند سمك 10 سم في طبقات كل من الغرين الرمادي (العينة G19 من مقطع كَلي) والمدملكات الحمراء (العينة Q18 من مقطع كالبازا). تُظهر طبقات G19 وQ18 محتوى منخفض من الكالسايت ووجود كل من الأنالسيم والسمكتايت والفيرميكيولايت. تم تسجيل شذوذات إيجابية لـ SiO_2 وAl_2O_3 وFe_2O_3 وMgO وNa_2O وK_2O وTTEs وZr وZn وCu، وشذوذات سلبية لـ CaO وMnO وLOI وHf وSr وCs عند طبقات G19وQ18 التي يبلغ سمكها 10 سم. تم الكشف أيضًا عن مستويات مرتفعة من Fe/Al وNi/Al وCr/Al وSO_2/MnO عند طبقات G19 وQ18. استناداً إلى الأدلة الحالية، فإن الحدود المقترحة لطبقات الغرين الرمادي (العينة G19) والمدملكات الحمراء (العينة Q18) من مقطعي كَلي وكالبازا على التوالي، يمكن أن تمثل حد الكريتاسي/الباليوجين (K/Pg)، مع احتمال تعرية أجزاءً منها.

DOI: 10.33899/injes.v26i1.60186,

Introduction

The K/Pg boundary event is currently one of the greatest contentious topics in geology due to the geochemical elemental anomalies related to these period deposits and environmental catastrophes caused the massive extinction that characterized the Cretaceous end before ~ 66 Ma, marking the end of the Mesozoic Era and the beginning of the Cenozoic Era. The Cretaceous period began 145 Ma ago and ended abruptly 66.04 Ma ago with the entrance of a new period of Paleogene that continued for 43 Ma (Coccioni and Silva, 2015). The geochemical and mineralogical anomalies across the K/Pg boundary at various places around the world were attributed to the impact of an extraterrestrial object with a diameter of 10 km on the Earth and/or the widespread, long-lasting activity of Deccan eruptions at the end of the Mesozoic (Alvarez et al., 1980; Adatte et al., 2002). Both a large asteroid-projectile (Chicxulub) impacted Earth in the Yucatán Peninsula of Mexico (mixed target) and the Deccan Traps eruptions in India caused worldwide fires, acidic rains, and dust fog-cloud that continued for a long time (Alvarez et al., 1980; Keller et al., 2012), which prevented sunlight and led to a global and abrupt fall in degrees of temperature that caused the disrubbery of the food system and mass extinction (Keller et al., 2011; Sial et al., 2019). The three events of Chicxulub impact, mass extinction, and giant pulse of Deccan eruptions possibly happened within a hundred thousand years of one another (Sial et al., 2019). Although the Chicxulub impact and Deccan volcanism were more than 13,000 km apart, they might have cooperatively contributed to the end-Cretaceous mass extinction (Renne et al., 2015).

Although biostratigraphical studies have been conducted on the K/Pg boundary in Iraq, mineralogical and geochemical research have made relatively few and limited contributions. Therefore, this paper aims to detect the K/Pg boundary between the Tanjero and Kolosh formations in northern and northeastern Iraq by mineralogical and geochemical anomalies.

Study area

The study area is situated in the Iraqi Kurdistan Region (IKR) at the governorates of Erbil and Sulaymaniyah in the northeast of Iraq (Table 1 and Fig. 1). The Gali section lies in the Sama Qulley area, approximately 55 km east of Erbil City, 36 km southeast of Shaqlawa Town, and 11 km north of Koysinjaq Town on the northeast limb of Awagird Mountain at the plunging of the Safeen anticline in the direction of southeast, and for a distance of 1 km southeast of the Gali Village. The Qalbaza section, on the other hand, is located in the Qalbaza Village at the southern boundary of Sharazoor Plain, which is about 41 km southeast of Sulaymaniyah City, 19 km northwest of Halabja City, 12 km southeast of Halebjai Taza Town, and 11 km northeast of the Darbandikhan Lake.

According to Buday and Jassim (1987), the study area sits within the High Folded Zone of the Unstable Shelf (Fig. 2). Moreover, Figure 3 shows the geological map of the studied sections in Erbil and Sulaymaniyah areas.

Table 1: Locations and coordination of the studied sections.

Governorate	Section	Latitude	Longitude	Nearby point
Erbil	Gali	36° 10′ 51.30″ N	44° 36′ 40.80″ E	Gali Village
Sulaymaniyah	Qalbaza	35° 15′ 41.34″ N	45° 48′ 27.06″ E	Qalbaza Village

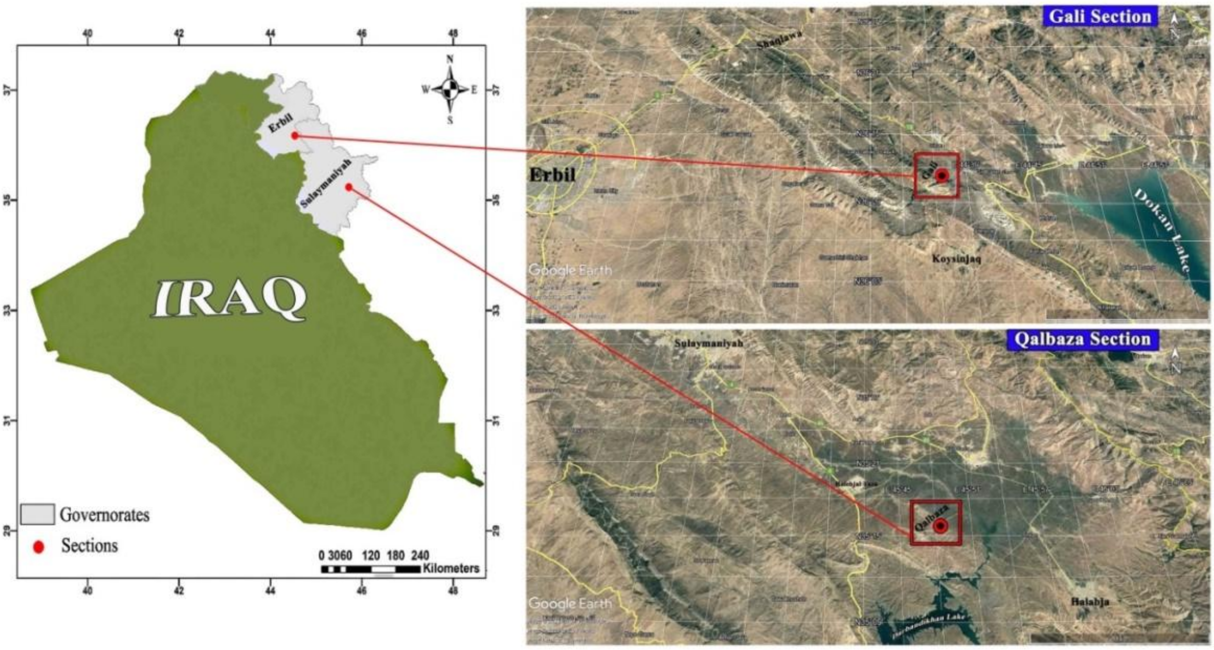

Fig. 1. Location of the studied sections.

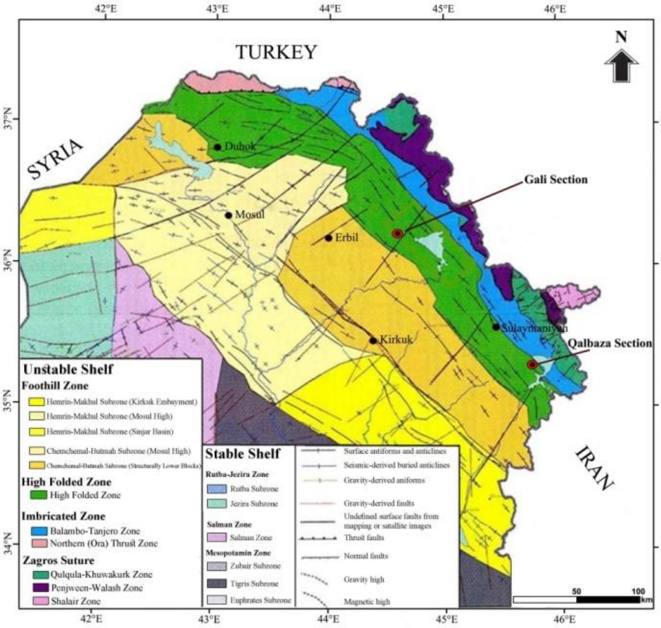

Fig. 2. Tectonic division map of Iraq showing the location of the studied area, modified from Buday and Jassim (1984).

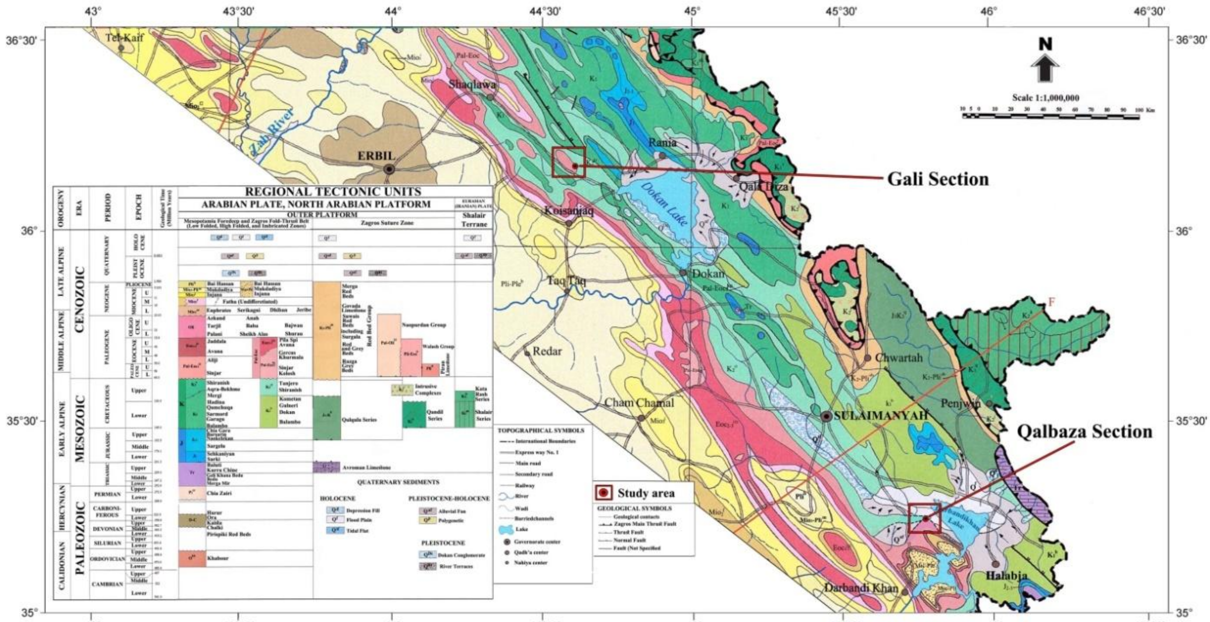

Fig. 3. Geological map of the studied area from Sissakian and Fouad (2012). The boundary between the Tanjero and Kolosh formations in the Qalbaza section has been modified.

Methodology

Fieldwork and sampling

The boundaries between the Tanjero and Kolosh formations have been proposed by the biostratigraphical studies of Sharbazheri (2008) in the Gali section and Al-Qayim et al. (2020) in the Qalbaza section. Based on changes in lithological characteristics and bed colors, 62 samples were collected (30 from the Gali section and 32 from the Qalbaza section) with sampling distances intensified to vary between 0.5 and 20 cm at the field-observed K/Pg boundary (possibly K/Pg).

However, fieldwork reveals that the total thickness of the Gali section is about 61.7 m (31.7 m for Tanjero Formation and 29.3 m for Kolosh Formation) (Fig. 4). The lower part of the Tanjero Formation conformably overlies gray shale interbedded with gray marl of the Shiranish Formation. On the other hand, the upper part of the Tanjero Formation ends with 10 cm of gray siltstone (sample G19) (Figs. 4 and 5). The K/Pg boundary was initially marked in the field within 70 cm of gray marly limestone (sample G20), which contains limestone ball structures with diameter range of 5–15 cm (Fig. 5). These structures may be located between the Tanjero and Kolosh formations due to slump and foundering of beds or deep burial by tectonic horizontal forces and differential load pressure (Potter and Pettijohn, 1977; Karim, 2004). The biostratigraphical study of Sharbazheri (2008) determined the K/Pg boundary within 1.25 m of 1 m of oily impregnated friable-soft and weathered pale brown fine sandstone beds and 25 cm of dark organic papery shale interlayered by thin beds of dark grey marl. This case is not observed in the current investigation. Moreover, Sharbazheri (2008) reported that the boundary was difficult to identify in the field due to an erosional surface and no continuous biostratigraphic document. In the Gali section, the lower part of the Kolosh Formation conformably overlies gray marly limestone; it consists of olive sandy marlstone (sample G21, 10 cm thick) overlaid by 20 cm of olive friable sandstone (sample G22) (Fig. 4).

On the other hand, the total thickness of the Qalbaza section is about 47 m, which consists of 26.5 m of Tanjero's upper part and 20.2 m of Kolosh's lower part (Fig. 6). The upper part ends with 20 cm of gray silty marlstone (sample Q16) (Figs. 6 and 7A). The K/Pg boundary was initially determined by the appearance of two conglomerate layers (20 cm of sample Q17 and 10 cm of sample Q18, respectively) (Figs. 6 and 7). These layers are overlaid by the first layer of the Kolosh Formation (sample Q19), which consists of 1 m of dark gray sandstone with sand ball structures (2–15 cm in diameter) (Figs. 6 and 7B). The sources of these structures were illustrated when the previous section was explained. The conglomerate reveals the unconformity contact between the Tanjero and the Kolosh formations (Abawi et al., 1982), and may be the submarine fans created the conglomerate during periodic tectonic activity pulses (Karim, 2004). The biostratigraphical study of Al-Qayim et al. (2020) determined the K/Pg boundary in the Qalbaza section within the marlstone layers with no break or hiatus.

Laboratory works

Many methods and techniques are used in this work, including insoluble residue (IR), pipette analysis, polarized microscopy, X-ray diffraction (XRD), fusion X-ray fluorescence (XRF), and inductively coupled plasma-mass spectrometry (ICP-MS). For selected samples across the K/Pg boundary, IR, pipette analysis, and a petrographic study were conducted in the geochemical laboratory, Geology Department, College of Science, University of Mosul. While in the laboratories of the Iranian University of Science and Technology (IUST), Tehran, the following techniques were carried out: XRD of PW3830 type for 13 samples (6 and 7 samples for Gali and Qalbaza section respectively); fusion XRF of PW1480 type for 11 samples (5 and 6 samples for Gali and Qalbaza section respectively); ICP-MS of Agilent 7700 series type for 13 samples (7 and 6 samples for Gali and Qalbaza section respectively); and fire assay-ICP-MS (to determine the platinum group elements (PGE)) for 7 samples (3 and 4 samples for Gali and Qalbaza section respectively).

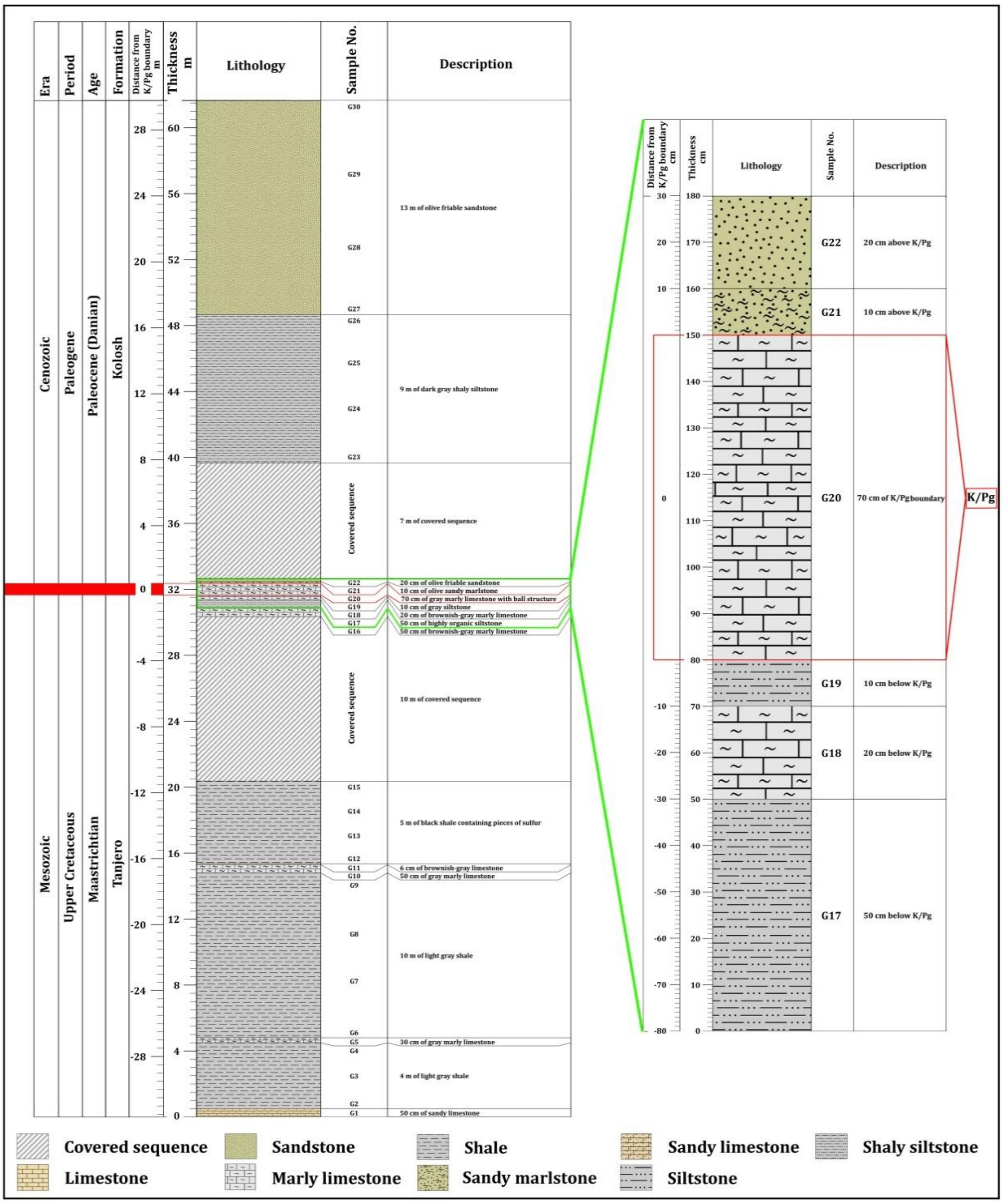

Fig. 4. Lithostratigraphic column across the K/Pg boundary in the Gali section.

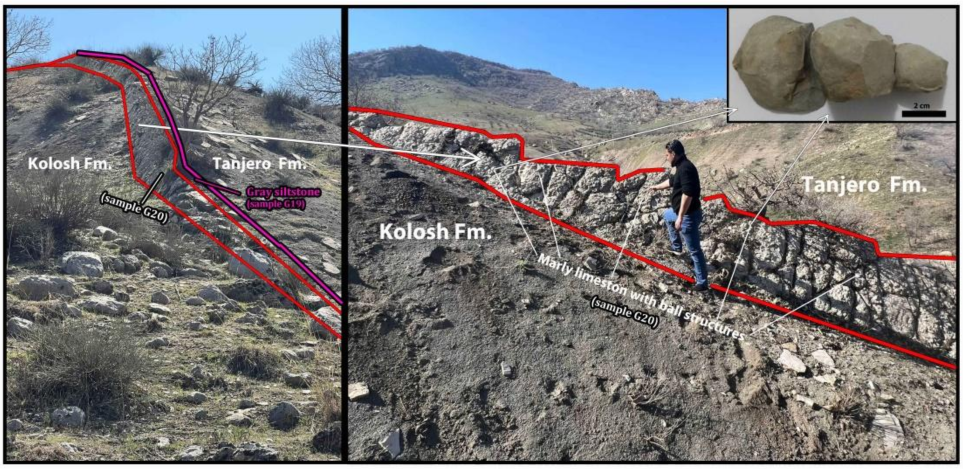

Fig. 5. Field photo from the Gali section showing the upper part of the Tanjero Formation (10 cm gray siltstone; sample G19) and the initial proposed K/Pg boundary (70 cm of marly limestone layer with ball structures; sample G20).

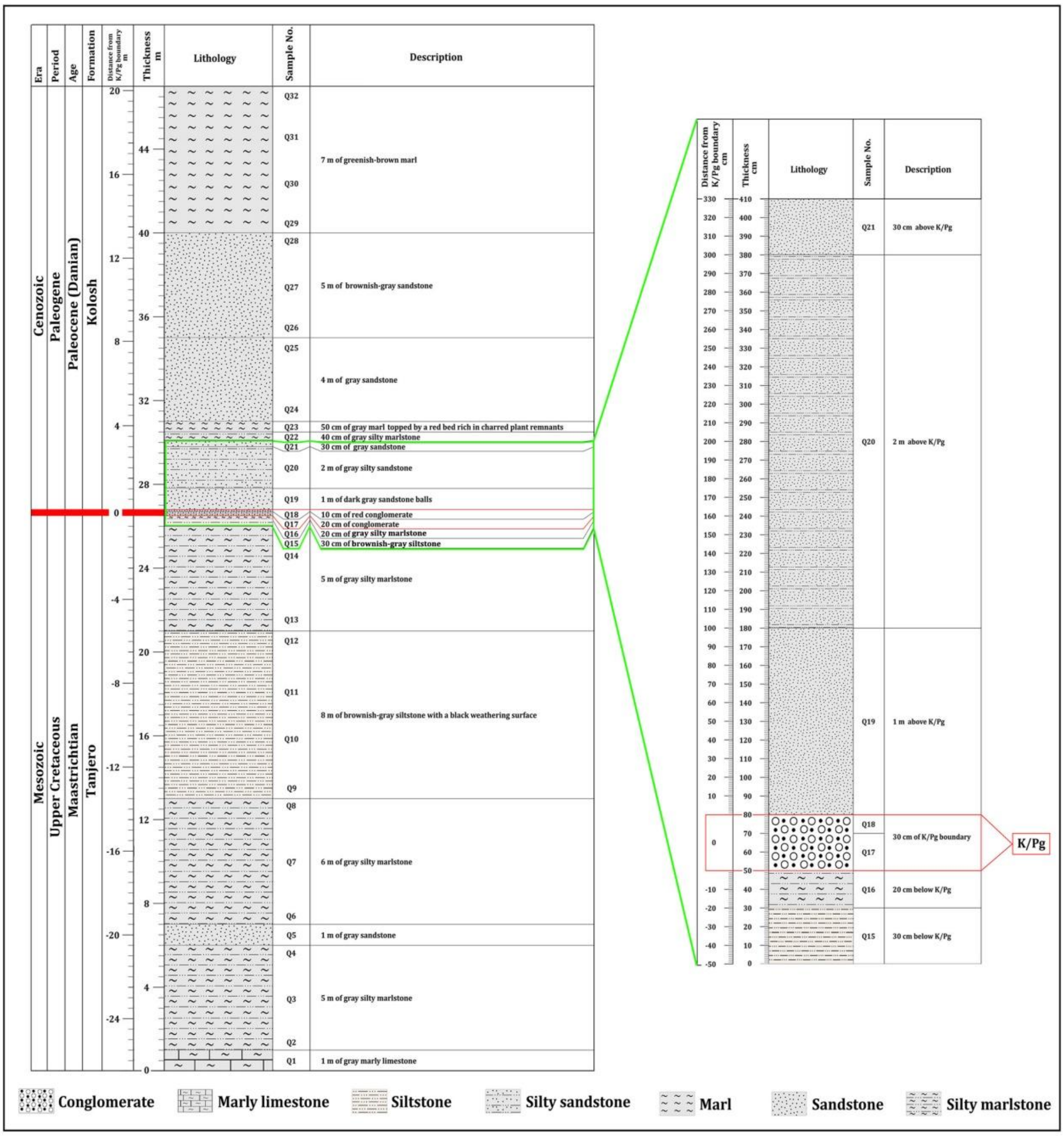

Fig. 6. Lithostratigraphic column across the K/Pg boundary in the Qalbaza section.

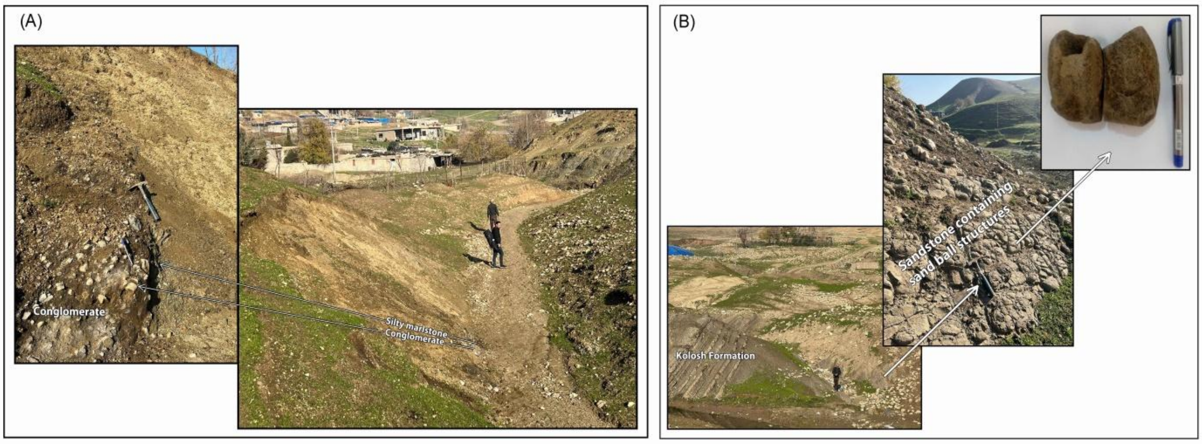

Fig. 7. Field photos from the Qalbaza section. (A) The upper part of the Tanjero Formation exhibiting 20 cm gray silty marlstone (sample Q16) with 30 cm conglomerates (samples Q17 and Q18). (B) The lower part of the Kolosh Formation displaying 1 m dark gray sandstone with sand ball structures (sample Q19).

Results and Discussion

Petrography

The petrographic study across the K/Pg boundary reveals that the Gali section comprises carbonates and sandstones. The carbonate petrography shows that sample G18 of the Upper Cretaceous consists of 10–50% globular planktonic foraminifera embedded in a micritic matrix (Fig. 8A and B) as planktonic foraminiferal lime wackestone microfacies (Dunham, 1962), which is consistent with the Tanjero microfacies that were classified by Al-Hamed and Malak (2021). On the other hand, sample G20 of the Lower Paleogene is composed of < 10% skeletal grains with about 90% micritic matrix (Fig. 8C) as fossiliferous lime mudstone microfacies (Dunham, 1962). Calcite, minor amounts of monocrystalline quartz, and iron oxides comprise the mineral composition of these two microfacies (Fig. 8 B, C, and D). The decline in foraminifera from Upper Cretaceous (~50%) to Lower Paleogene (<10%) layers could be associated with the Chicxulub impact and/or Deccan events (Smit, 1982; Keller et al., 2011), which caused one of the greatest mass extinctions (Petersen et al., 2016; Bardeen et al., 2017). After this event, little species began to emerge (Smit, 1982; Arenillas et al., 2004). Therefore, the K/Pg boundary in the Gali section could be the layer of sample G19 set between the increase and decrease in assemblages.

Sandstone constituents of the Gali and Qalbaza sections are given in Tables 2 and 3. Two varieties of quartz grains were determined, mono- and polycrystalline (Fig. 9A and B). The proposed K/Pg layers show the highest total quartz content compared to the samples below and above these boundaries (Tables 2 and 3). Quartz influx increases at K/Pg layers as sea level falls (Bourgeois et al., 1988; Smit, 1999). Both sections show a minor amount of feldspars (Tables 2 and 3; Fig. 9C and D) due to their high susceptibility to chemical breakdown during weathering and diagenetic processes to form clays (Pettijohn, 1975; Boggs, 2006). Moreover, orthoclase dominates over plagioclase in the studied samples because orthoclase is more stable during chemical weathering (Nichols, 2009). Rock fragments mainly comprise carbonate with minor amounts of chert, igneous, and metamorphic rock fragments (Fig. 9E and F; Fig. 10A and B), indicating that the Gali and Qalbaza sandstones derived from older, highly carbonate-containing formations exposed to the surface through tectonic processes (Dickinson, 1985; Zattin and Zuffa, 2004). The proposed K/Pg layers contained the lowest amount of carbonate fragments (Tables 2 and 3). Gali and Qalbaza sandstones included a high matrix proportion (Tables 2 and 3) with carbonate cement dominating these sandstones (Fig. 10A), as well as low amounts of heavy minerals such as iron oxide, hornblende, and pyroxene (Tables 2 and 3; Fig. 10A, B, C, and D). Fig. 11 shows the petrographic variation across the proposed K/Pg boundaries of the Gali (sample G19) and Qalbaza (sample Q18) sections. These boundaries reveal a decrease in carbonate rock fragments, chert, and heavy minerals, while an increase in total quartz and K-feldspar. Calcite cement increases significantly in samples located above the boundaries. Moreover, maximum matrix content can be observed at the Qalbaza K/Pg boundary and below the Gali K/Pg boundary. Detrital component variations at the boundary are possibly due to elevated global environmental stress during the Upper Cretaceous, which resulted from volcanism in the Deccan trap before the Chicxulub impact (Font et al., 2018). Consequently, samples G19 and Q18 from the Gali and Qalbaza sections could indicate the K/Pg boundary. Despite this, detecting the K/Pg boundary cannot only be done by a petrographic study. This necessitates the contribution of mineralogical and geochemical proof to determine or propose the boundary layer.

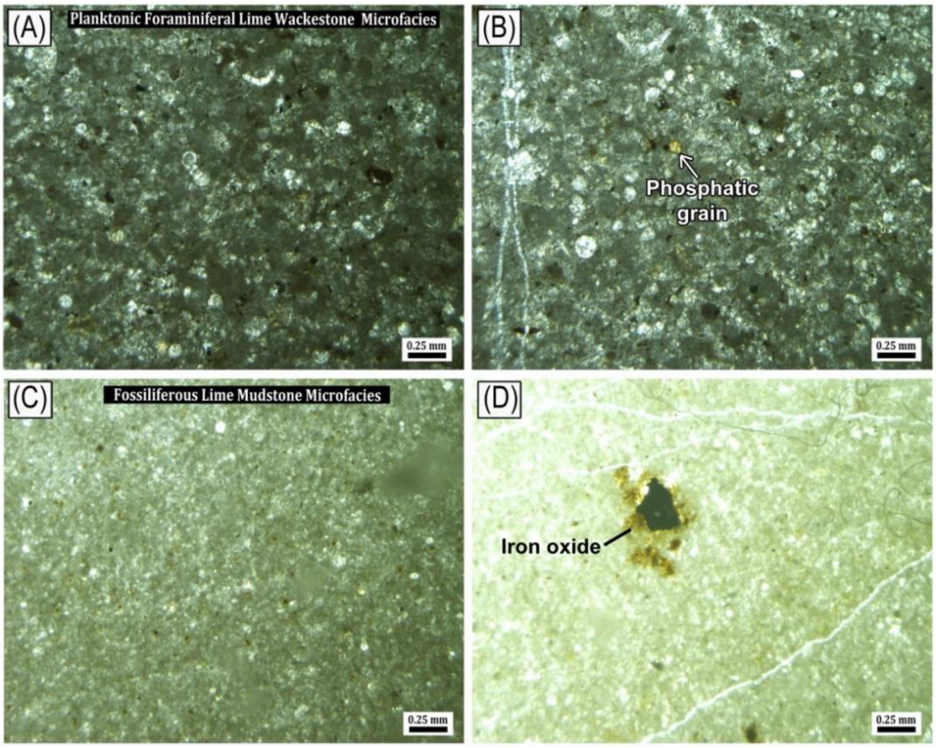

Fig. 8. Photomicrographs of Gali section carbonate samples. (A) Planktonic foraminiferal lime wackestone microfacies; sample G18 (40X). (B) Globular planktonic foraminifera, phosphatic grain, and monocrystalline quartz; sample G18 (40X). (C) Fossiliferous lime mudstone; sample G20 (40X). (D) Iron oxide; sample G20 (40X).

Table 2: The major petrographic components % of the Gali section.

Components	G22	G21	G19 (K/Pg)	G17	Min.	Max.	Average
Monocrystalline	10.50	8.00	14	11.5	8.00	14.00	11.00
Polycrystalline	2.00	2.50	5	1	1.00	5.00	2.63
K-feldspar	0.00	0.50	1	0	0.00	1.00	0.38
Plagioclase	0.00	0.50	0.5	0	0.00	0.50	0.25
Carbonate	36.00	34.00	32	35	32.00	36.00	34.25
Chert	4.50	1.50	0	0.5	0.00	4.50	1.63
Igneous and metamorphic	4.00	0.50	1	0.5	0.50	4.00	1.50
Heavy minerals	1.00	1.00	0.5	2	0.50	2.00	1.13
Matrix	37.00	34.00	36	41.5	34.00	41.50	37.13
Cement	5.00	17.50	10	8	5.00	17.50	10.13
Total	100	100	100	100			100
Quartz (Q %)	21.93	22.11	35.51	25.77	21.93	35.51	26.33
Feldspar (F %)	0.00	2.11	2.80	0.00	0.00	2.80	1.23
Rock Fragment (RF%)	78.07	75.79	61.68	74.23	61.68	75.79	72.44

Table 3: The major petrographic components % of the Qalbaza section.

Components	Q21	Q20	Q19	Q18 (K/Pg)	Q17	Q16	Q15	Min.	Max.	Average
Monocrystalline	20.50	12.00	11.50	15.00	9.00	16.5	18.25	9.00	20.50	14.68
Polycrystalline	5.25	3.50	2.50	3.00	0.50	1	2.5	0.50	5.25	2.61
K-feldspar	2.00	1.50	0.50	1.25	0.50	1.5	3	0.50	3.00	1.46
Plagioclase	1.00	1.50	1.00	1.50	2.50	2	1	1.00	2.50	1.50
Carbonate	23.50	28.00	26.50	18.00	39.00	32.5	27	18.00	39.00	27.79
Chert	4.50	2.00	7.50	3.00	4.50	1.5	2.25	1.50	7.50	3.61
Igneous and metamorphic	3.00	5.50	3.50	0.00	0.50	2	4.5	0.00	5.50	2.71
Heavy minerals	1.00	2.00	1.00	0.50	1.00	2.5	2	0.50	2.50	1.43
Matrix	36.00	42.50	40.00	56.25	41.00	35.25	38	35.25	56.25	41.29
Cement	3.25	1.50	6.00	1.50	1.50	5.25	1.5	1.50	6.00	2.93
Total	100	100	100	100	100	100	100			100
Quartz (Q %)	43.10	28.70	26.42	43.11	16.81	30.70	35.47	16.81	43.11	32.04
Feldspar (F %)	5.02	5.56	2.83	6.59	5.31	6.14	6.84	2.83	6.84	5.47
Rock Fragment (RF %)	51.88	65.74	70.75	50.30	77.88	63.16	57.69	50.30	77.88	62.49

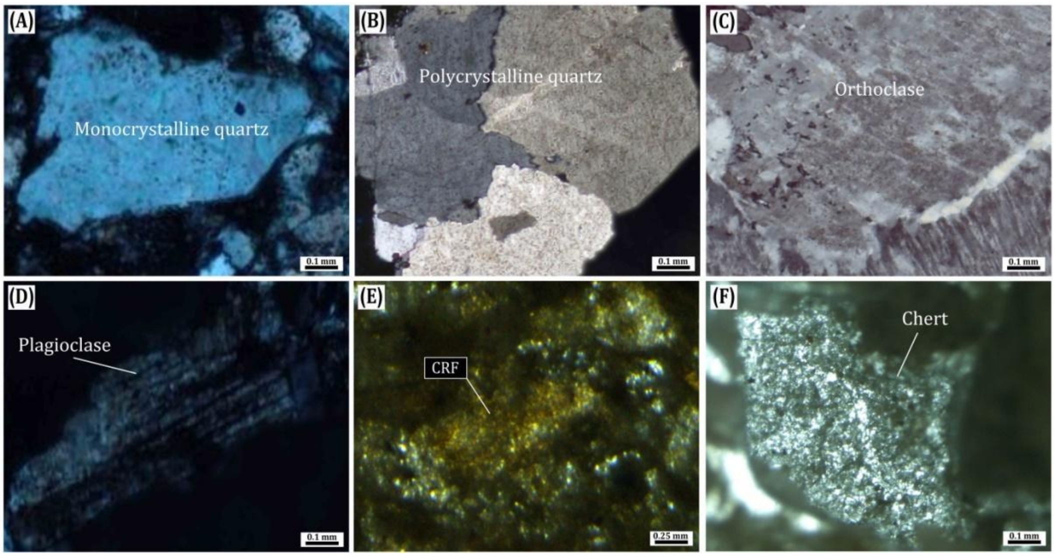

Fig. 9. Photomicrographs of Gali and Qalbaza sandstones. (A) Monocrystalline quartz; sample Q18 (100X; XPL). (B) Polycrystalline quartz; sample G19 (100X; XPL). (C) Orthoclase feldspar; sample Q15 (100X; XPL). (D) Plagioclase feldspar; sample Q18 (100X; XPL). (E) Carbonate rock fragments (CRF); sample Q21 (40X; PPL). (F) Chert rock fragment; sample G22 (100X; PPL).

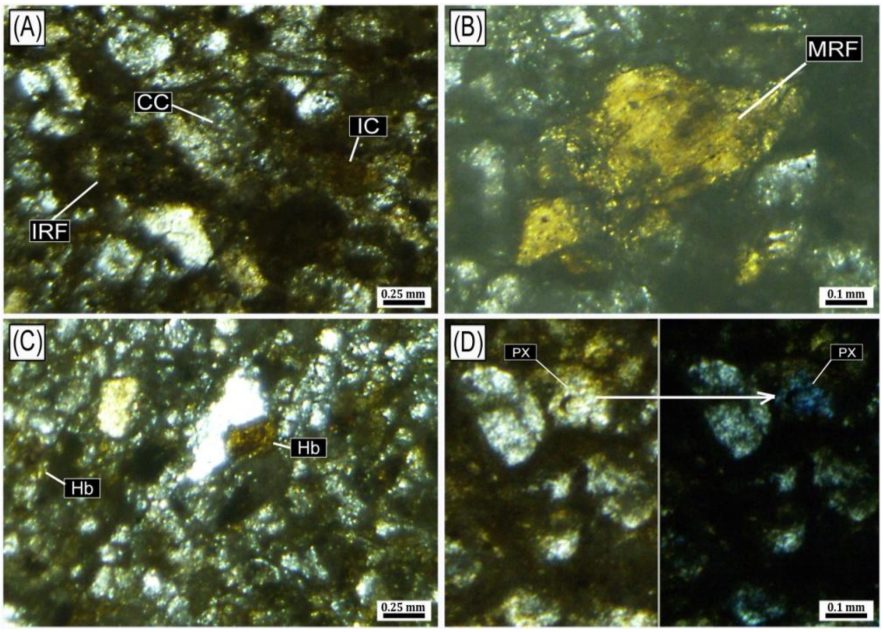

Fig. 10. Photomicrographs of Gali and Qalbaza sandstones. (A) Igneous rock fragments (IRF), carbonate cement (CC), and iron cement (IC); sample G21 (40X; PPL). (B) Metamorphic rock fragments; sample G17 (100X; PPL). (C) Hornblende (Hb); sample Q15 (40X; PPL). (D) Pyroxene (PX); sample Q20 (100X; PPL on left and XPL on right).

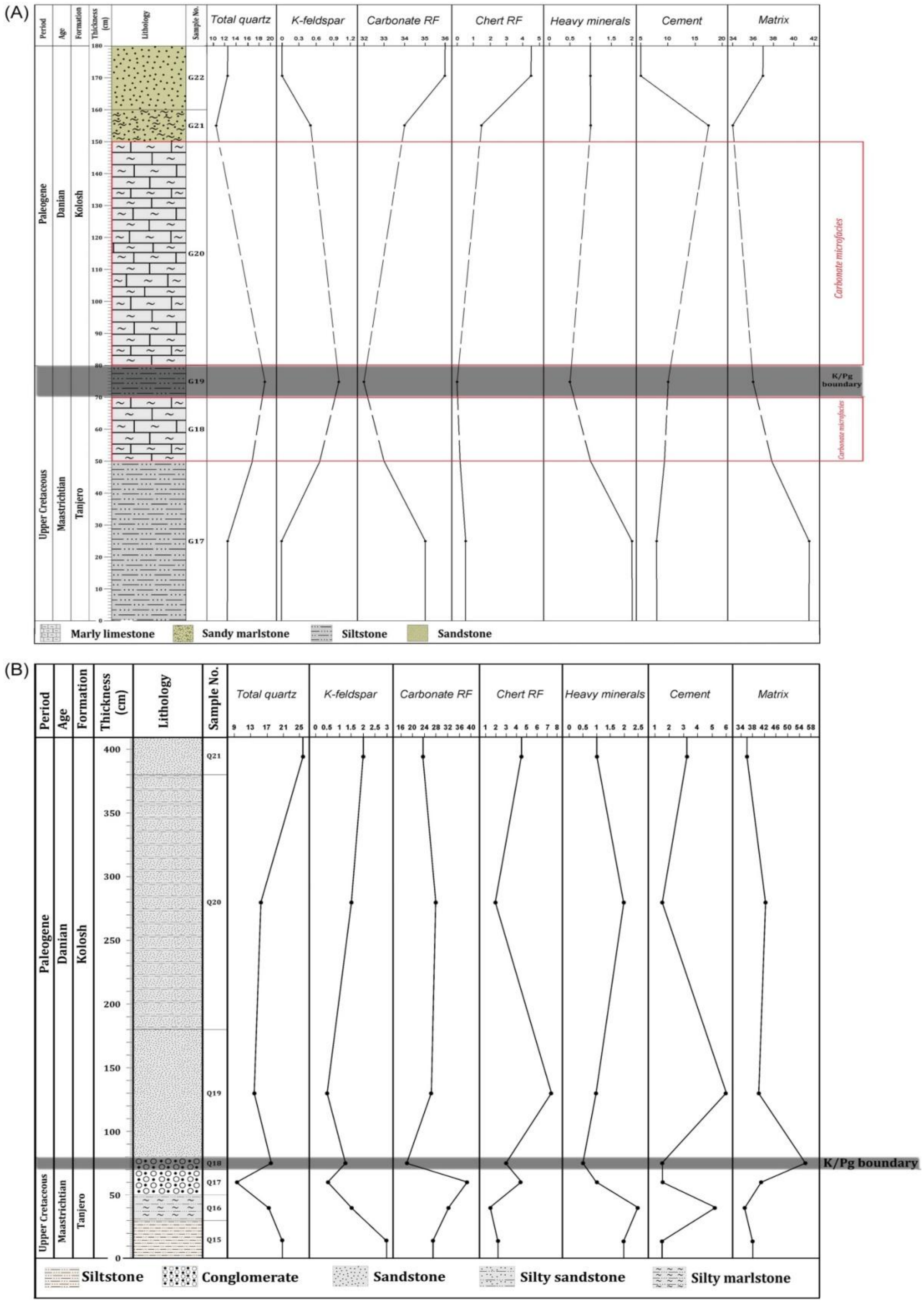

Fig. 11. Petrographic variation across the K/Pg boundary from (A) Gali section and (B) Qalbaza section.

According to Pettijohn (1975), Gali and Qalbaza sandstones are considered texturally immature due to their over 15% matrix content (Tables 2 and 3). The mineralogical maturity index (MMI) in the Gali and Qalbaza sandstones was calculated (Tables 4 and 5) using the MMI = Q / (F + RF) equation and parameters in Table 6 proposed by Nwajide and Hoque (1985). MMI values are between 0.28 and 0.55 with an average of 0.37 for Gali sandstones and between 0.20 and 0.76 with an average of 0.50 for Qalbaza sandstones (Tables 4 and 5). These calculated MMI values correspond to the categories Q = < 50% and MMI ≤ 1 in Table 6, indicating that the Gali and Qalbaza sandstones are immature sediments.

According to Dott (1964), Gali and Qalbaza sandstones are classified as lithic graywacke sandstones (Fig. 12).

Table 4: Modal composition of the sandstone and mineralogical maturity index (MMI) in the Gali section.

Components	G22	G21	G19 (K/pg)	G17	Min.	Max.	Average
Quartz (Q)	12.50	10.50	19.00	12.50	10.50	19.00	13.63
Feldspar (F)	0.00	1.00	1.50	0.00	0.00	1.50	0.63
Rock Fragment (RF)	44.50	36.00	33.00	36.00	33.00	44.50	37.38
Total	57.00	47.50	53.50	48.50	47.50	57.00	51.63
F + RF	44.50	37.00	34.50	36.00	34.50	44.50	38.00
Q %	21.93	22.11	35.51	25.77	21.93	35.51	26.33
F + RF %	78.07	77.89	64.49	74.23	64.49	78.07	73.67
MMI %	0.28	0.28	0.55	0.35	0.28	0.55	0.37

Table 5: Modal composition of the sandstone and mineralogical maturity index (MMI) in the Qalbaza section.

Components	Q21	Q20	Q19	Q18 (K/pg)	Q17	Q16	Q15	Min.	Max.	Average.
Quartz (Q)	25.75	15.50	14.00	18.00	9.50	17.50	20.75	9.50	25.75	17.29
Feldspar (F)	3.00	3.00	1.50	2.75	3.00	3.50	4.00	1.50	4.00	2.96
Rock Fragment (RF)	31.00	35.50	37.50	21.00	44.00	36.00	33.75	21.00	44.00	34.11
Total	59.75	54.00	53.00	41.75	56.50	57.00	58.50	41.75	59.75	54.36
F + RF	34.00	38.50	39.00	23.75	47.00	39.50	37.75	23.75	47.00	37.07
Q %	43.10	28.70	26.42	43.11	16.81	30.70	35.47	16.81	43.11	32.04
F + RF %	56.90	71.30	73.58	56.89	83.19	69.30	64.53	56.89	83.19	67.96
MMI %	0.76	0.40	0.36	0.76	0.20	0.44	0.55	0.20	0.76	0.50

Table 6: Maturity scale of sandstones shows limiting % of Q, (F + RF), and MMI stage (Nwajide and Hoque, 1985).

Q = ≥ 95% , (F + RF) = 50%	MMI = ≥ 19 Super mature
Q = 95-90% , (F + RF) = 5-10%	MMI = 19-9.0 Sub mature
Q = 90-75% , (F + RF) = 10-25%	MMI = 9.0-3.0 Sub mature
Q = 75-50% , (F + RF) = 25-50%	MMI = 3.0-1.0 Immature
Q = < 50%	MMI ≤ 1 Immature
(F + RF) > 50%	Extremely immature

Abbreviations: Q (quartz%), F (feldspars%), RF (rock fragments%), and MMI (mineralogical maturity index).

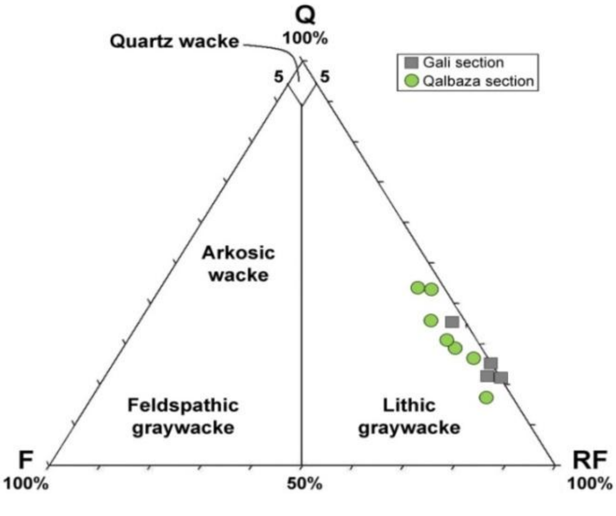

Fig. 12. Sandstone classification of the Gali and Qalbaza samples (Dott, 1964). Q (quartz), F (feldspar), and RF (rock fragments).

Furthermore, the Q-F-L ternary diagram (Fig. 13 A) illustrates that most of the Gali samples are plotted in the undissected arc field, excluding one sample (G19) in the recycled orogenic field, whereas four samples (Q15, Q16, Q18, and Q21) of the Qalbaza sandstones are plotted in the recycled orogenic field, two samples (Q19 and Q20) in the transition area between recycled orogenic and transitional arc fields, and one sample (Q17) in the undissected arc field. Moreover, the Qm-F-Lt ternary diagram (Fig. 13 B) indicates that the Gali and Qalbaza sandstones were derived from a recycled orogenic provenance. Weathered products of the elevated orogenic belt are moved to the nearby foreland basins (Dickinson and

Suczek, 1979; Dickinson, 1985; Al-Hamidi et al., 2023). As is the case in the foreland basins located on the passive margin of the Arabian Plate, which received their sediments from the northern and northeastern eroded margins of the Arabian Plate's collision zone with the Turkish-Iranian Plate, hence Tanjero and Kolosh formations are believed to be sourced from sedimentary, igneous, and metamorphic rocks (Jassim and Goff, 2006; Al-Hamidi et al., 2023). Tanjero and Kolosh source area is situated to the northeast of the basin, where tectonic forces caused this area to rise and move to the northeast, and Tanjero and Kolosh flysch deposits are a result of the Zagros Foreland Basin's creation by elevating older sedimentary rocks (Çelik and Salih, 2021). Hence, ophiolites of the Zagros suture zone, Qulqula group, and Avroman Formation carbonates were potential sources for Gali and Qalbaza sandstones. Moreover, the current study indicates that the Gali and Qalbaza sandstones were deposited in an arid to semi-arid paleoclimate (Fig. 14).

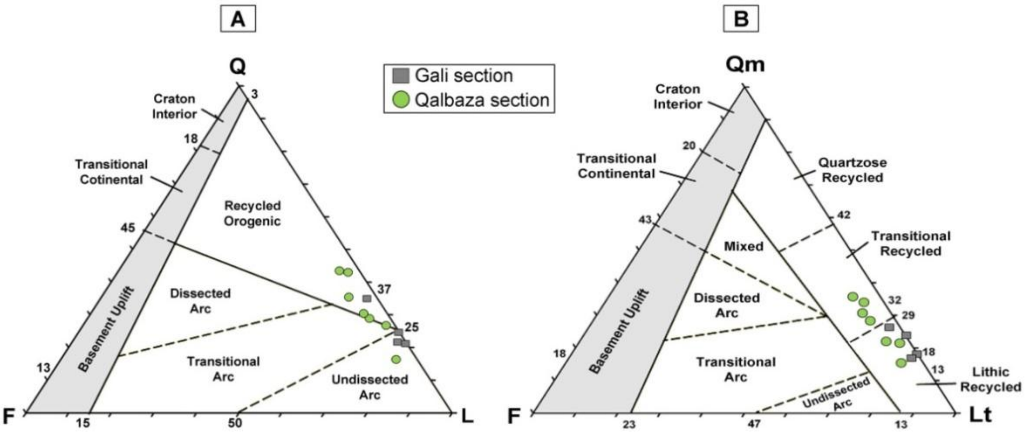

Fig. 13. Tectonic provenance ternary diagrams of Gali and Qalbaza sandstones. (A) Q-F-L (Ingersoll and Suczek, 1979). (B) Qm-F-Lt (Dickinson and Suczek, 1979). Q (quartz), F (feldspar), L (rock fragments), Qm (monocrystalline quartz), and Lt (rock fragments + polycrystalline quartz).

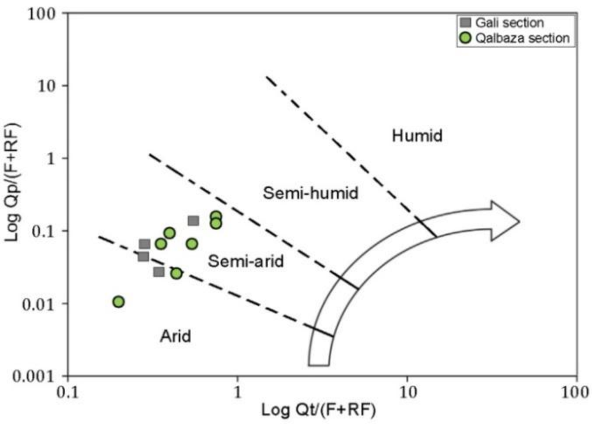

Fig. 14. Paleoclimate diagram of sandstone samples from the Gali and Qalbaza sections (Suttner and Dutta, 1986). Qt (total quartz), Qp (polycrystalline quartz), F (feldspars), and RF (rock fragments).

Mineralogy

Generally, the mineralogical composition of the Gali section is dominated by calcite, quartz, and clay minerals (Fig. 15). Sample layer G20 (carbonate facies) was proposed as the K/Pg boundary in the Gali section based on the field criteria; however, the petrographic study revealed that sample G19 may represent the K/Pg boundary; unfortunately, sample G18 was not analyzed by XRD.

In the Qalbaza section, the mineralogical composition mainly consists of quartz, calcite, and clay minerals with minor amounts of plagioclase, analcime, and muscovite (Fig. 16). Sample Q18 was proposed as the K/Pg boundary in this section based on the petrographic study. Tables 7, 8, 9, and 10 show the semi-quantitative mineralogical proportions in the Gali and Qalbaza sections by calculating the area under the peak of reflection according to the method suggested by Carver (1971).

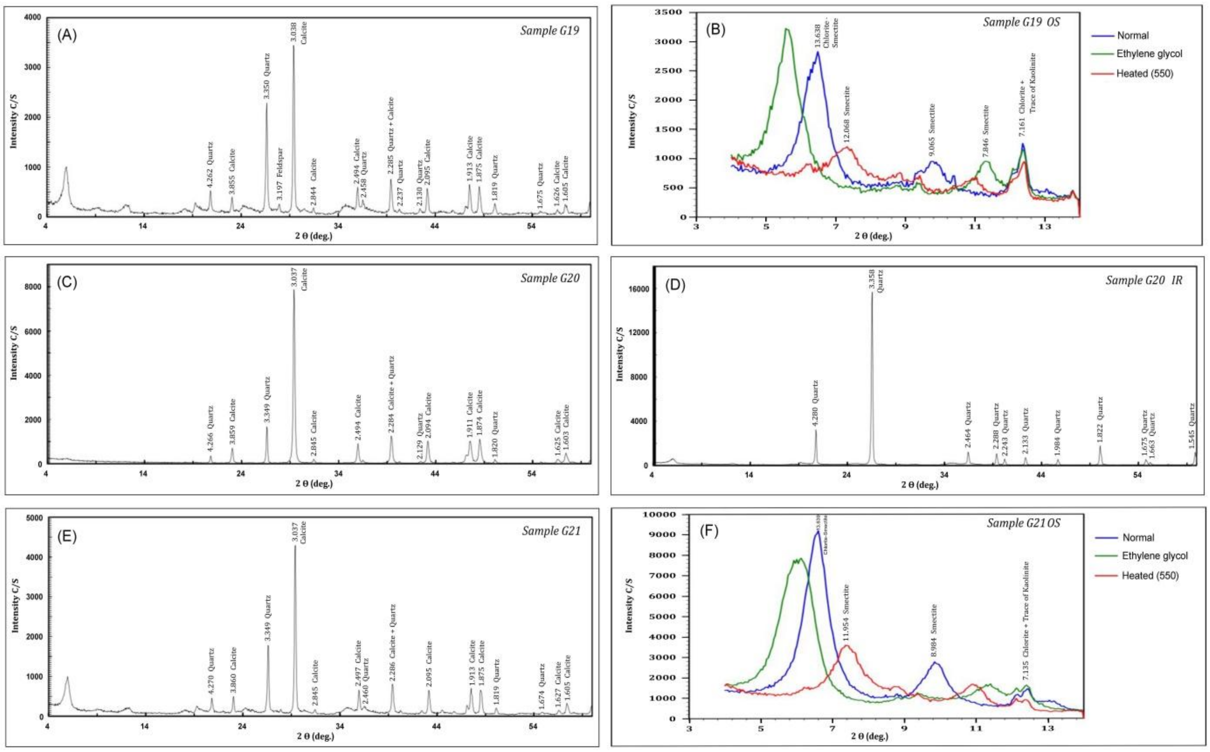

Fig. 15. XRD pattern of Gali section. (A) Bulk sample G19. (B) Oriented slide of sample G19 (G19 OS). (C) Bulk sample G20. (D) Sample G20 was processed by the insoluble residues method. (E) Bulk sample G21. (F) Oriented slide of sample G21 (G21 OS). (A) and (B) represent the proposed K/Pg boundary; (C), (D), (E), and (F) represent the Paleogene layers.

Table 7: Semi-quantitative bulk mineralogical proportions in the Gali section.

Mineralogy	**Bulk Samples**			**The sample was processed by the insoluble residues method (IR)**
	G21	**G20**	**G19**	**G20 IR**
Calcite %	79.53	89.84	49.79	—
Quartz %	20.47	10.16	48.88	100
Feldspar %	—	—	1.33	—
Total	100	100	100	100

Table 8: Semi-quantitative clay mineral proportions in the Gali section.

Mineralogy	**G21OS**	**G19OS**
Chlorite-Smectite %	91.73	68.32
Smectite %	5.99	20.13
Chlorite + Kaolinite %	2.28	11.55
Total	100	100

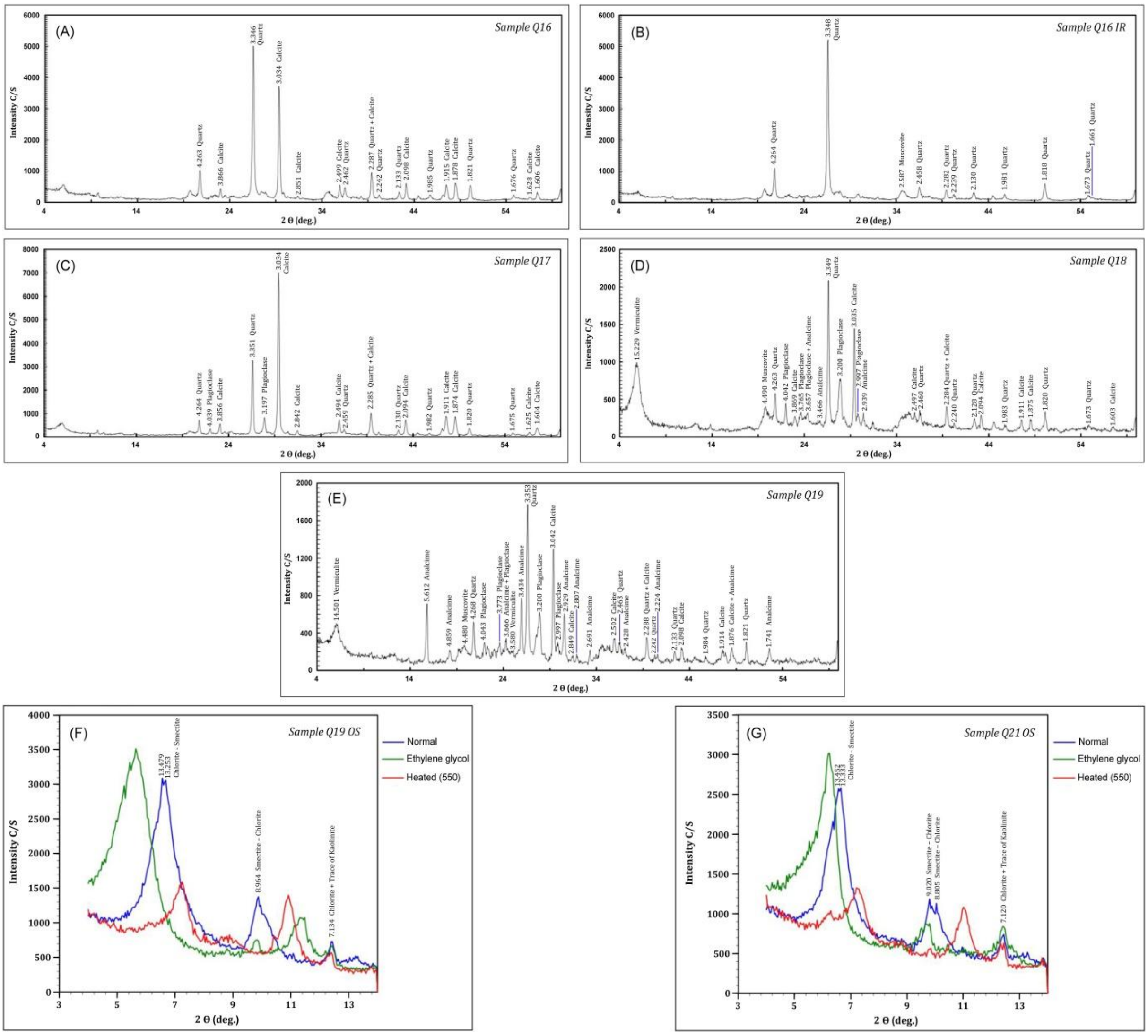

Fig. 16. XRD pattern of Qalbaza section. (A) Bulk sample Q16. (B) Sample Q16 was processed by the insoluble residues method. (C) Bulk sample Q17. (D) Bulk sample Q18. (E) Bulk sample Q19. (F) Oriented slide of sample Q19 (Q19OS). (G) Oriented slide of sample Q21 (Q21OS). (A), (B), and (C) represent the Upper Cretaceous layers; (D) represents the proposed K/Pg boundary; (E), (F), and (G) represent the Paleogene layers.

Table 9: Semi-quantitative bulk mineralogical proportions in the Qalbaza section.

Mineralogy	Bulk Samples				The sample was processed by the insoluble residues method (IR)
	Q19	Q18	Q17	Q16	Q16 IR
Quartz %	36.42	40.74	24.94	51.73	95.44
Calcite %	23.76	13.98	71.17	48.27	—
Vermiculite %	8.04	28.63	—	—	—
Plagioclase %	15.13	11.16	3.89	—	—
Analcime %	14.62	2.04	—	—	—
Muscovite %	2.03	3.45	—	—	4.56
Total	100	100	100	100	100

Table 10: Semi-quantitative clay mineral proportions in the Qalbaza section.

Mineralogy	Q21OS	Q19OS
Chlorite-Smectite %	95.76	96.97
Chlorite + Kaolinite %	4.24	3.03
Total	100	100

In the Gali section, the proposed K/Pg boundary (sample G19) possesses the lowest calcite (49.79%) and highest quartz (48.88%), where calcite increases to 89.84% and quartz decreases to 10.16% at the Lower Paleogene layer (sample G20) after the proposed K/Pg boundary (Table 7). In the Qalbaza section, calcite decreases, and quartz increases within the proposed K/Pg layer (sample Q18), then calcite increases and quartz decreases at the Lower Paleogene layer (sample Q19) (Table 9). The lowest content or sharp decrease in the calcite, which corresponds to carbonate rock fragments decreasing (see petrography topic), at the Gali and Qalbaza K/Pg boundaries may be attributed to the change of conditions caused by Chicxulub and/or Deccan events, such as acidic rain and global temperature drops, etc., that might have cooperatively contributed to temporarily preventing the development of biogenic calcite by dissolved or inhibition of planktonic carbonate (Keller et al., 2011). Moreover, the high levels of quartz, which are consistent with the petrography study, at the K/Pg boundaries of both sections may be attributed to a quartz influx increase as sea level falls during the K/Pg event (Bourgeois et al., 1988; Smit, 1999). Analcime was diagnosed at both the K/Pg boundary and the Lower Paleogene layers (samples Q18 and Q19, respectively) of the Qalbaza section. It is a low-temperature phase that can be a replacement product from vitric tuffs, cement of pyroclastic rocks, or spherules of silica glass as an authigenic mineral in the sediments (Gribble and Hall, 1985; Liou et al., 1991). Analcime occurs in terrestrial deposits under warm, arid to semi-arid environments (Iijima and Utada, 1966; Liou et al., 1991). This phase was found at the K/Pg boundary and/or the Lower Paleogene layer in Taringatura of New Zealand (Coombs, 1954), Chicxulub impact crater (Kring et al., 2020), Western Argentina (Montano et al., 2023), and Alabama in the USA (Pitakpaivan et al., 1994). Therefore, analcime presence at both the K/Pg boundary layer and the Lower Paleogene layers of the Qalbaza section may be attributed to the Deccan eruptions and/or Chicxulub impact event.

Clay minerals of Gali and Qalbaza sections across the proposed K/Pg boundary are dominated by smectite (montmorillonite), chlorite-smectite mixed layer, chlorite + trace of kaolinite, and vermiculite (Figs. 15 B, F; 16 D, E, F, G, and Tables 8, 9, 10). The K/Pg boundary (sample G19OS) of the Gali section has a higher smectite content than the Paleogene layer (sample G21OS) (Table 8). Smectite minerals are formed by the weathering of igneous and metamorphic rocks in a semi-arid climate and alkaline water with restricted water movement (Carroll, 1970). Smectite usually reflects volcanic activities; it can be derived from a volcanic ash submarine alteration during a devitrification process (Harder, 1972). Smectite can also be derived from spherules associated with the Mexico ‘‘Chicxulub’’ impact, where the spherules may be completely replaced by smectite, calcite, or chlorite (Mateo et al., 2019), like Demerara Rise in western North Atlantic, La Sierrita in NE Mexico, and Brazos River in Texas (Mateo et al., 2019). The Gali section's Paleogene layer (sample G21OS) has higher chlorite-smectite content than the K/Pg boundary (sample G19OS) (Table 8), while the Qalbaza section's Paleogene layers (samples Q19OS and Q21OS) show a significant chlorite-smectite mixed layer (Table 10). Temperature increases cause smectite to change gradually into chlorite (Horton, 1985), indicating temperatures were restored after the K/Pg event. A significant amount of vermiculite was determined at the K/Pg boundary (sample Q18) of the Qalbaza section (Fig. 16D and Table 9). Vermiculite arises essentially from the weathering of biotite and muscovite under arid conditions (Pal et al., 1989; Srivastava et al., 1998). Vermiculite was one clay mineral identified at the K/Pg boundary between the Tanjero and Kolosh formations around Sulaimani City, Iraq (Mustafa et al., 2022).

The proposed K/Pg boundaries of both studied sections are mineralogically characterized by the low calcite, high quartz, analcime, and clay minerals of smectite and vermiculite, so they resemble all other global well-known K/Pg boundaries, such as Stevns Klint in Denmark, Blake Nose in the NW Atlantic, Agost and Caravaca in Spain, and Gubbio in Italy. Additionally, the proposed K/Pg boundaries of both studied sections differ from these typical K/Pg boundaries due to the absence of spherules and shocked quartz related to the Chicxulub event; this may be attributed to the spherules being completely replaced by smectite, calcite, or chlorite and the disappearance of shocked quartz grains gradually with distance from the Chicxulub crater (Joanna et al., 2006), similar to the K/Pg boundaries of Hermanas hill section in western Cuba (Jorge et al., 2015) and Medetli and Gölpazari sections in northwestern Turkey (Yoji et al., 2003). Therefore, the mineralogical results indicate that the G19 and Q18 layers of the Gali and Qalbaza sections, respectively, may represent the K/Pg boundaries, while not excluding the idea that part of these boundaries may have been eroded.

Geochemistry

The chemical composition of major, trace, and rare earth elements is given in Tables 11 and 12. Chondrite-normalized REE patterns (Fig. 17) exhibit similarity with each other and show a one-package zigzag pattern; this may reflect a single melt that suffered from differentiation to provide the source rocks from which sediments were derived. Generally, the REE pattern differs from UCC and PAAS patterns and displays more enrichment than chondrite and slightly enriched light rare earth elements (LREEs) relative to heavy rare earth elements (HREEs) (Tables 11 and 12; Fig. 17), as well as elevated Tb and Tm, suggesting the REE scavenging mechanism from seawater (De Baar et al., 1985). Moreover, the sediments show positive Eu and slightly negative Ce anomalies in most samples (Tables 11 and 12; Fig. 17). The Eu anomaly is exhibited by transitioning from Eu^{3+} to Eu^{2+} under reducing conditions (Brookins, 1989). Positive Eu anomalies ($Eu/Eu^* > 1$) have often been caused by plagioclase feldspar accumulation during magmatic differentiation (Trubelja et al., 1995), so the positive anomaly may be due to the absence and/or slight presence of plagioclase in the studied samples. The soluble Ce^{3+} oxidation to less soluble Ce^{4+} is responsible for the negative Ce anomaly ($Ce/Ce^* < 1$) (Sholkovitz et al., 1994). Positive Eu/Eu* and slightly negative Ce/Ce* (Tables 11 and 12; Fig. 17) may suggest that the studied sediments were deposited under oxic-anoxic paleoredox conditions.

The K/Pg boundaries of Gali and Qalbaza sections are shared by a prominent positive anomaly for SiO_2, Al_2O_3, Fe_2O_3, MgO, Na_2O, K_2O, TTEs ‘‘transition trace elements’’ (Ni, Co, Cr, Sc, and V), Zr, Zn, and Cu and a prominent negative anomaly for CaO, MnO, LOI, Hf, Sr, and Cs (Figs. 18-21). The K/Pg boundary layers around the world often contain elevated concentrations of SiO_2, Al_2O_3, Fe_2O_3, MgO, Na_2O, K_2O, TiO_2, Ni, Co, Cr, Sc, V, Zr, Zn, and Cu (Alvarez et al., 1980; Smit and ten Kate, 1982; Vajda and Wigforss-Lange, 2006). Therefore, proponents of the impact theory propose that the asteroid and target zone are the source of these elements (Smit and ten Kate, 1982; Gilmour and Anders, 1989), and advocates of volcanic activity theory argue that these elements are derived from the post-fallout from the Deccan cloud (Graup et al., 1989). SiO_2, Al_2O_3, Fe_2O_3, MgO, Na_2O, and K_2O elements elevate during the K/Pg event due to vegetation decreases or sea-level fall, causing the ground to become unstable and further prone to erosional stages (Bercovici et al., 2012).

Table 11: Concentrations of major oxides (in wt%), trace elements (in ppm), and rare earth elements (in ppm) of the Gali section. Major oxides were analyzed by XRF; trace and rare earth elements were analyzed by ICP-MS. * Major oxides were analyzed by ICP-MS.

	G23	G22	G21	G20	G19 (K/Pg)	G18	G17*	Min.	Max.	Average
SiO_2		44.43	37.32	11.02	40.92	26.57		11.02	44.43	32.05
Al_2O_3	6.67*	8.48	6.11	1.01	7.48	2.66	>5.0*	1.01	8.48	5.40
Fe_2O_3	>5.0*	7.29	6.20	0.89	6.76	3.24	>5.0*	0.89	7.29	4.88
MgO	>5.0*	10.54	8.73	1.35	8.87	5.47	>5.0*	1.35	10.54	6.99
CaO	>5.0*	9.78	17.74	46.65	13.97	31.61	>5.0*	9.78	46.65	23.95
Na_2O	0.47*	0.30	0.11	0.38	0.22	0.21	1.47*	0.11	1.47	0.45
K_2O	0.60*	0.64	0.27	0.03	0.45	0.03	0.52*	0.03	0.64	0.36
TiO_2	0.27*	0.337	0.233	0.044	0.269	0.132	0.43*	0.04	0.43	0.25
P_2O_5	0.04*	0.07	0.08	0.04	0.06	0.05	0.04*	0.04	0.08	0.05
MnO	0.07*	0.132	0.115	0.242	0.122	0.135	0.08*	0.07	0.242	0.13
LOI		17.82	22.89	38.07	20.64	29.66		17.82	38.07	25.82
Total		99.82	99.80	99.73	99.76	99.77				
Ni	1110	717	562	64	598	201	827	64	1110	582.71
Co	88.24	78.67	36.68	6.72	58.27	15.78	85.94	6.72	88.24	52.90
Cr	677	418	226	22	299	63	531	22	677	319.43
Sc	19.8	25.1	16.2	2.1	19.4	6.8	32.9	2.1	32.9	17.47

V	91	119	76	17	93	33	136	17	136	80.71
Zr	71	68	92	<1	71	17	19	1	92	48.43
Hf	10.36	9.25	8.65	8.58	10.25	11.06	12.01	8.58	12.01	10.02
Nb	4.69	5.85	6.47	7.85	7.89	6.21	5.45	4.69	7.89	6.34
Ta	3.58	5.96	3.58	4.25	3.41	5.78	6.01	3.41	6.01	4.65
Th	6.25	9.21	8.25	10.25	7.65	9.74	8.25	6.25	10.25	8.51
U	2.58	1.41	3.12	6.58	4.62	4.25	2.54	1.41	6.58	3.59
Y	14.25	15.36	15.21	11.25	16.54	13.25	18.52	11.25	18.52	14.91
Ba	6147.8	1610.3	622.3	3.2	1212.3	19.2	27.3	3.2	6147.8	1377.49
Rb	14.36	16.25	17.85	13.25	11.25	14.25	13.25	11.25	17.85	14.35
Sr	198.1	234.4	328	336.1	316.7	539.6	144	144	539.6	299.56
Cs	7.14	6.25	9.01	6.58	7.58	9.59	8.21	6.25	9.59	7.77
Li	23	36	28	9	34	23	33	9	36	26.57
Ga	5.41	2.25	1.26	2.14	4.26	3.85	1.14	1.14	5.41	2.90
Pb	333.25	4.26	1.25	6.25	7.21	1.45	3.25	1.25	333.25	50.99
Ag	0.74	0.32	3.01	0.25	0.41	0.31	0.41	0.25	3.01	0.78
As	8	7	8	3	4	5	2	2	8	5.29
Be	0.28	0.34	0.64	0.89	0.25	0.41	0.89	0.25	0.89	0.53
Bi	3.25	3.07	2.01	1.47	1.25	6.21	1.25	1.25	6.21	2.64
Cd	0.47	0.62	0.14	0.25	0.56	0.14	0.21	0.14	0.62	0.34
In	0.21	0.78	0.25	0.41	0.36	0.48	0.85	0.21	0.85	0.48
Mo	1.03	0.24	1.07	1.65	0.12	1.4	0.23	0.12	1.65	0.82
S	1800	500	300	200	500	500	300	200	1800	585.71
Sb	3.58	3.25	2.58	1.47	1.25	2.85	3.58	1.25	3.58	2.65
Sn	1.89	5.32	4.98	9.95	3.58	10.47	2.52	1.89	10.47	5.53
Te	0.34	0.58	0.74	0.48	0.36	0.85	0.24	0.24	0.85	0.51
Tl	3.25	1.85	2.54	2.14	3.21	3.25	2.14	1.85	3.25	2.63
W	1.25	6.25	7.45	2.85	3.62	6.25	2.58	1.25	7.45	4.32
Cu	39.1	57.1	44.6	7.1	48.2	27.3	59.1	7.1	59.1	40.36
Zn	63.6	78.8	56.3	8.1	66.2	22.5	64.9	8.1	78.8	51.49
La	5.15	5.96	6.96	4.64	8.09	6.32	3.12	3.12	8.09	5.75
Ce	11.25	12.36	14.25	10.36	17.65	13.58	6.21	6.21	17.65	12.24
Pr	2.98	1.71	2.69	2.03	3.28	2.26	1.03	1.03	3.28	2.28
Nd	6.23	4.69	4.89	3.79	6.89	4.69	2.26	2.26	6.89	4.78
Sm	4.49	3.26	3.21	3.21	3.01	2.12	1.03	1.03	4.49	2.90
Eu	3.03	2.31	2.26	2.29	2.01	1.03	0.69	0.69	3.03	1.95
Gd	4.12	3.19	4.58	3.69	2.89	1.89	0.95	0.95	4.58	3.04
Tb	2.89	2.03	2.12	2.59	1.03	0.91	0.43	0.43	2.89	1.71
Dy	3.89	3.01	3.59	3.39	2.21	1.59	0.69	0.69	3.89	2.62
Ho	2.42	1.71	1.49	2.49	0.79	0.69	0.31	0.31	2.49	1.41
Er	3.59	2.68	3.03	3.26	1.89	1.49	0.51	0.51	3.59	2.35
Tm	2.12	1.39	1.12	2.13	0.41	0.51	0.23	0.23	2.13	1.13
Yb	3.12	2.12	2.59	2.95	1.29	1.31	0.47	0.47	3.12	1.98
Lu	1.78	1.03	0.79	1.89	0.31	0.36	0.12	0.12	1.89	0.90
LREE	33.13	30.29	34.26	26.32	40.93	30.00	14.34	14.34	40.93	29.90
HREE	23.93	17.16	19.31	22.39	10.82	8.75	3.71	3.71	23.93	15.15
LREE/HREE	1.38	1.77	1.77	1.18	3.78	3.43	3.87	1.18	3.87	2.45
ΣREE	57.06	47.45	53.57	48.71	51.75	38.75	18.05	18.05	57.06	45.05
(La/Sm)*n*	0.74	1.18	1.40	0.93	1.74	1.92	1.96	0.74	1.96	1.41
(Gd/Yb)*n*	1.09	1.24	1.46	1.03	1.85	1.19	1.67	1.03	1.85	1.36
(La/Yb)*n*	1.18	2.02	1.93	1.13	4.50	3.46	4.76	1.13	4.76	2.71
Eu/Eu*	2.16	2.19	1.80	2.04	2.09	1.58	2.14	1.58	2.19	2.00
Ce/Ce*	0.70	0.95	0.81	0.83	0.84	0.88	0.85	0.70	0.95	0.84

Table 12: Concentrations of major oxides (in wt%), trace elements (in ppm), and rare earth elements (in ppm) of the Qalbaza section. Major oxides were analyzed by XRF; trace and rare earth elements were analyzed by ICP-MS.

	Q21	Q19	Q18 (K/Pg)	Q17	Q16	Q15	Min.	Max.	Average
SiO_2	63.64	53.44	55.71	33.95	56.25	58.84	33.95	63.64	53.64
Al_2O_3	9.78	10.28	9.89	7.31	8.7	10.49	7.31	10.54	9.41
Fe_2O_3	4.34	7.85	7.55	3.3	4.17	5.26	3.30	7.85	5.41
MgO	2.8	5.64	3.49	1.76	2.68	3.14	1.76	5.64	3.25
CaO	5.83	7.24	6.73	28.22	10.31	7.77	5.83	28.22	11.02
Na_2O	1.36	0.72	1.63	0.63	0.17	0.45	0.17	1.63	0.83
K_2O	0.41	1.35	0.66	0.21	2.01	1.51	0.21	2.01	1.03
TiO_2	0.438	0.62	0.586	0.246	0.345	0.434	0.25	0.62	0.44
P_2O_5	0.057	0.056	0.038	0.062	0.106	0.087	0.04	0.11	0.07
MnO	0.064	0.119	0.078	0.334	0.085	0.07	0.06	0.33	0.13
LOI	11.12	12.41	12.99	23.84	14.97	11.66	11.12	23.84	14.50
Total	99.84	99.73	99.35	99.86	99.80	99.71			
Ni	74	64	90	60	68	64	60	90	70
Co	35.18	38.36	38.14	29.41	22.03	26.55	22.03	38.36	31.61
Cr	65	87	128	40	40	42	40	128	67
Sc	25.3	34.1	31.4	13.7	16.2	21.2	13.7	34.1	23.65

V	138	206	186	118	95	133	95	206	146
Zr	54	57	56	49	108	98	49	108	70.33
Hf	10.36	9.36	8.14	9.85	12.05	11.36	8.14	12.05	10.19
Nb	3.25	3.14	4.62	5.52	4.69	2.85	2.85	5.52	4.01
Ta	3.25	5.89	4.58	6.09	3.58	4.78	3.25	6.09	4.70
Th	9.25	10.36	11.25	10.36	9.54	4.85	4.85	11.25	9.27
U	3.74	2.78	3.58	6.35	4.87	3.69	2.78	6.35	4.17
Y	15.01	14.85	12.58	13.25	11.25	17.21	11.25	17.21	14.03
Ba	89.3	261.1	127.5	2909.6	3347.9	4795.6	89.3	4795.6	1921.83
Rb	13.85	17.25	19.21	13.69	14.25	13.25	13.25	19.21	15.25
Sr	128.8	484.3	145.6	290.1	503	328.6	128.8	503	313.4
Cs	9.85	7.85	5.98	8.14	9.21	6.28	5.98	9.85	7.89
Li	26	30	42	20	23	24	20	42	27.5
Ga	5.41	3.25	2.41	1.69	1.78	3.52	1.69	5.41	3.01
Pb	1.21	0.12	1.25	512.32	287.36	113.25	0.12	512.32	152.59
Ag	0.74	0.85	0.62	0.52	0.25	0.65	0.25	0.85	0.61
As	2	5	3	4	1	3	1	5	3
Be	0.47	0.89	0.74	0.65	1.44	0.74	0.47	1.44	0.82
Bi	4.05	1.32	1.25	6.03	1.85	1.58	1.25	6.03	2.68
Cd	0.52	0.21	0.14	0.36	0.14	0.52	0.14	0.52	0.32
In	0.45	0.31	0.36	0.14	0.62	0.25	0.14	0.62	0.36
Mo	2.25	0.21	0.14	1.04	0.21	1.22	0.14	2.25	0.85
S	900	1200	1300	2100	1000	1500	900	2100	1333.33
Sb	1.54	1.23	1.23	1.25	2.47	3.45	1.23	3.45	1.86
Sn	3.21	2.36	6.54	5.48	2.25	3.64	2.25	6.54	3.91
Te	0.52	0.47	0.91	0.68	0.18	0.52	0.18	0.91	0.55
Tl	3.25	4.14	3.25	2.58	1.78	1.25	1.25	4.14	2.71
W	93.61	34.21	45.48	60.29	5.25	4.25	4.25	93.61	40.52
Cu	37.4	95.1	35.2	26.4	55.9	65.1	26.4	95.1	52.52
Zn	37.8	73.9	43.3	31.6	70.6	64.3	31.6	73.9	53.58
La	6.12	6.36	4.14	10.20	16.67	16.45	4.14	16.67	9.99
Ce	12.01	11.25	9.21	21.25	32.25	31.25	9.21	32.25	19.54
Pr	1.29	2.12	1.89	6.36	8.96	9.25	1.29	9.25	4.98
Nd	4.23	4.21	2.89	8.48	13.25	12.69	2.89	13.25	7.63
Sm	3.26	3.03	2.03	6.25	7.96	8.69	2.03	8.69	5.20
Eu	2.36	2.14	1.23	5.01	7.03	6.25	1.23	7.03	4.00
Gd	3.96	3.02	2.58	6.18	10.58	9.09	2.58	10.58	5.90
Tb	2.12	2.03	1.03	4.56	6.25	5.36	1.03	6.25	3.56
Dy	3.25	2.89	2.12	5.39	9.36	8.03	2.12	9.36	5.17
Ho	1.89	1.58	0.91	3.78	5.15	5.03	0.91	5.15	3.06
Er	3.21	2.48	1.59	5.05	7.58	7.51	1.59	7.58	4.57
Tm	1.26	1.23	0.51	3.01	4.25	4.36	0.51	4.36	2.44
Yb	2.58	2.29	1.21	3.78	6.31	6.96	1.21	6.96	3.86
Lu	0.96	0.89	0.32	2.15	3.25	3.25	0.32	3.25	1.80
LREE	29.27	29.11	21.39	57.55	86.12	84.58	21.39	86.12	51.34
HREE	19.23	16.41	10.27	33.90	52.73	49.59	10.27	52.73	30.36
LREE/HREE	1.52	1.77	2.08	1.70	1.63	1.71	1.52	2.08	1.74
ΣREE	48.50	45.52	31.66	91.45	138.85	134.17	31.66	138.85	81.69
$(La/Sm)_n$	1.21	1.36	1.32	1.05	1.35	1.22	1.05	1.36	1.25
$(Gd/Yb)_n$	1.27	1.09	1.76	1.35	1.38	1.08	1.08	1.76	1.32
$(La/Yb)_n$	1.70	1.99	2.45	1.94	1.89	1.70	1.70	2.45	1.95
Eu/Eu*	2.01	2.17	1.65	2.47	2.34	2.15	1.65	2.47	2.13
Ce/Ce*	1.05	0.75	0.81	0.65	0.65	0.62	0.62	1.05	0.75

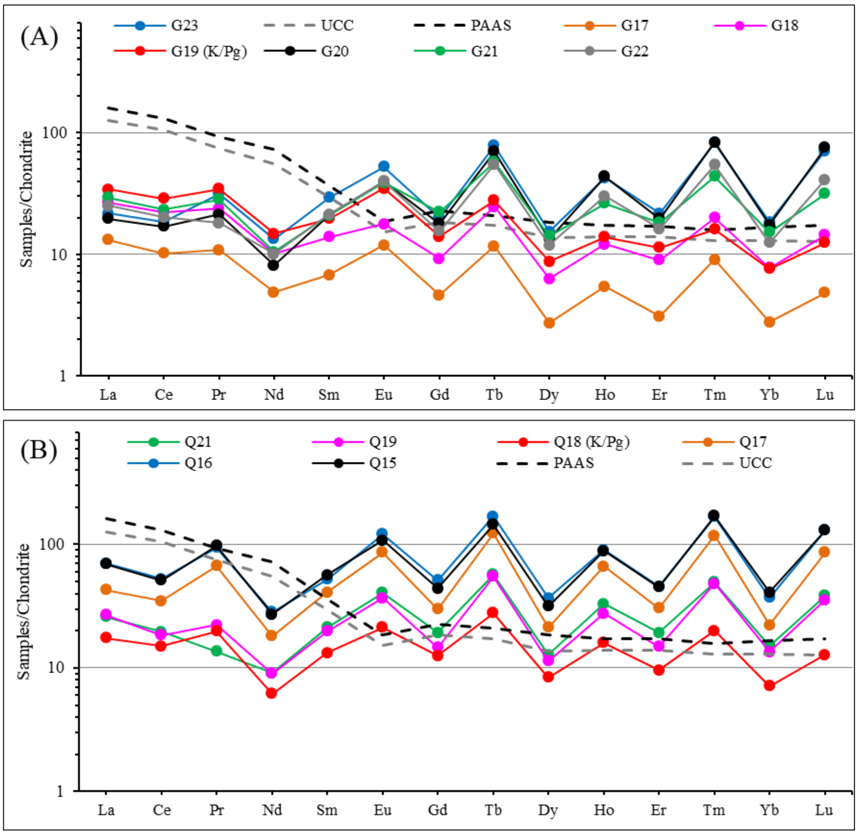

Fig. 17. Chondrite-normalized REE pattern of sediments across the K/Pg boundary in (A) Gali section and (B) Qalbaza section. Chondrite values are taken from Sun and McDonough (1989), and PAAS and UCC from Taylor and McLennan (1985).

Ni and Cr are two of the key elements to detect a K/Pg boundary (Smit and ten Kate, 1982), where high levels of Ni and Cr at the K/Pg boundary layer may be generated by an extraterrestrial origin (Smit and ten Kate, 1982). Furthermore, the elevated authigenic concentrations (element/Al) of Fe, Ni, and Cr within the proposed K/Pg layers of Gali and Qalbaza sections (Table 13) are a good indicator of these boundaries (Sosa-Montes de Oca et al., 2013; 2020). In addition, the elevated contents of Zr, Zn, and Cu may suggest that these elements derived from the rocks that were the Chicxulub target, or possibly derived from the post-fallout from the Deccan cloud (Premovic et al., 2004; Vajda and Wigforss-Lange, 2006). The Chicxculub fireball vapor cloud and/or Deccan eruptions cloud could produce an atmospheric acidity condition due to the release of amounts of SO_2, causing acidity rainfall (Prinn and Fegley, 1987), and this results in a higher SO_2/MnO ratio at the K/Pg boundary layer relative to prior and post layers (Keller, 2014; Renne et al., 2015). The K/Pg boundaries of the Gali and Qalbaza sections (samples G19 and Q18) exhibit a high SO_2/MnO ratio compared to the prior and post layers (Table 13).

PGEs anomaly proves the K/Pg boundary (Alvarez et al., 1980). Unfortunately, PGEs were undetected (< 5 pbb) in 3 samples of the Gali section (samples G19, G20, and G21) and 4 samples of the Qalbaza section (samples Q16, Q17, Q18, and Q19). As a result, this work suggests that PGEs may not be detectable at concentrations less than 5 ppb in Iraqi K/Pg boundary sites.

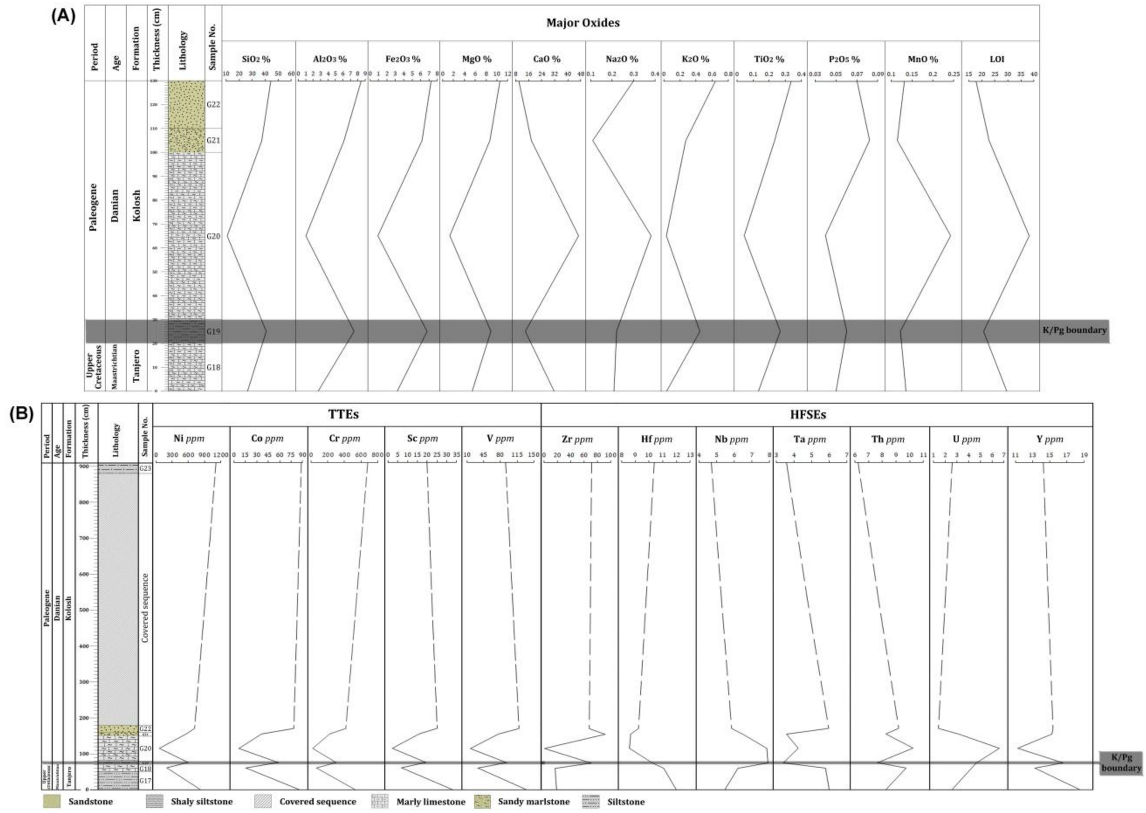

Fig. 18. Vertical distribution profile plot across the K/Pg boundary from the Gali section. (A) Major oxides with LOI. (B) Transition trace elements (TTEs) and high field strength elements (HFSEs). The gray area represents the K/Pg boundary layer.

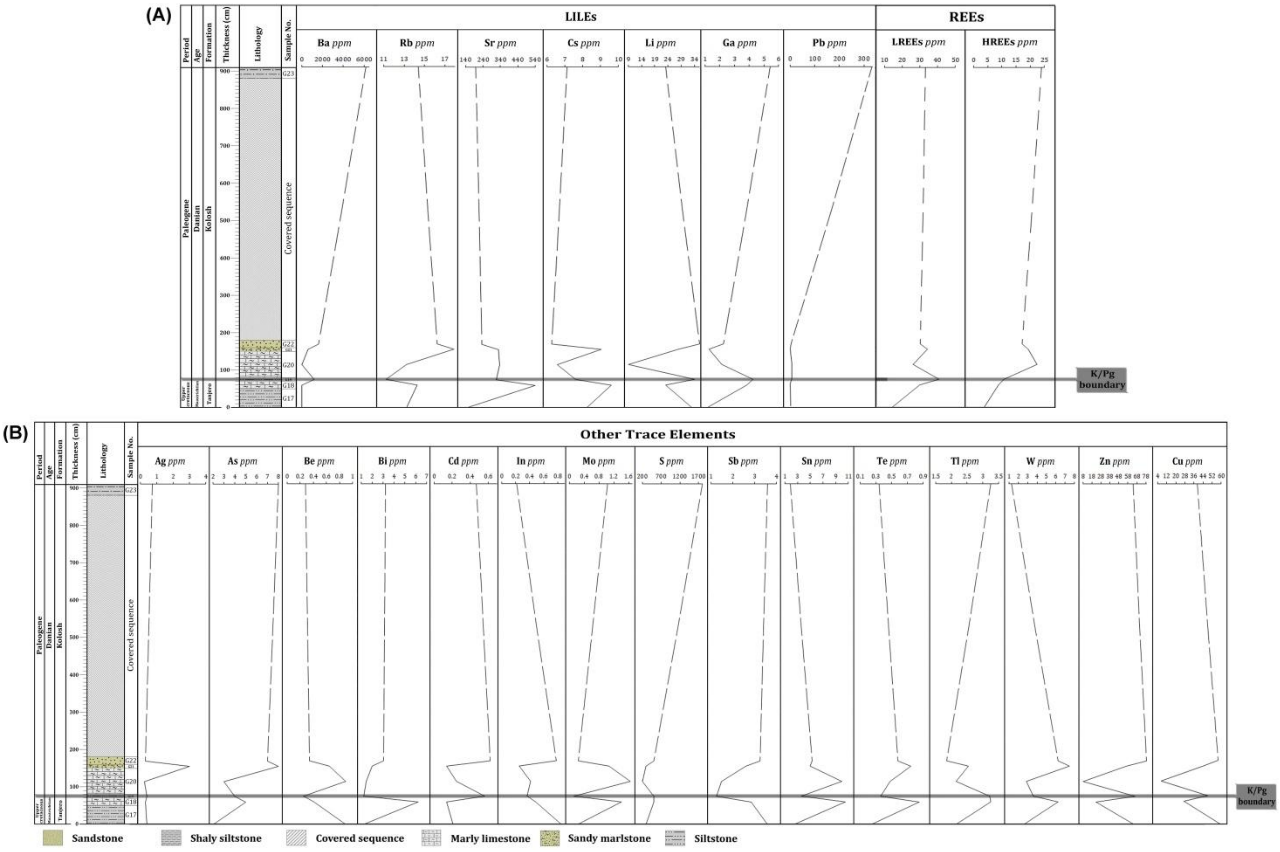

Fig. 19. Vertical distribution profile plot across the K/Pg boundary from the Gali section. (A) Large ion lithophile elements (LILEs), Light rare earth elements (LREEs), and heavy rare earth elements (HREEs). (B) Ag, As, Be, Bi, Cd, In, Mo, S, Sb, Sn, Te, Tl, W, Zn, and Cu elements. The gray area represents the K/Pg boundary layer.

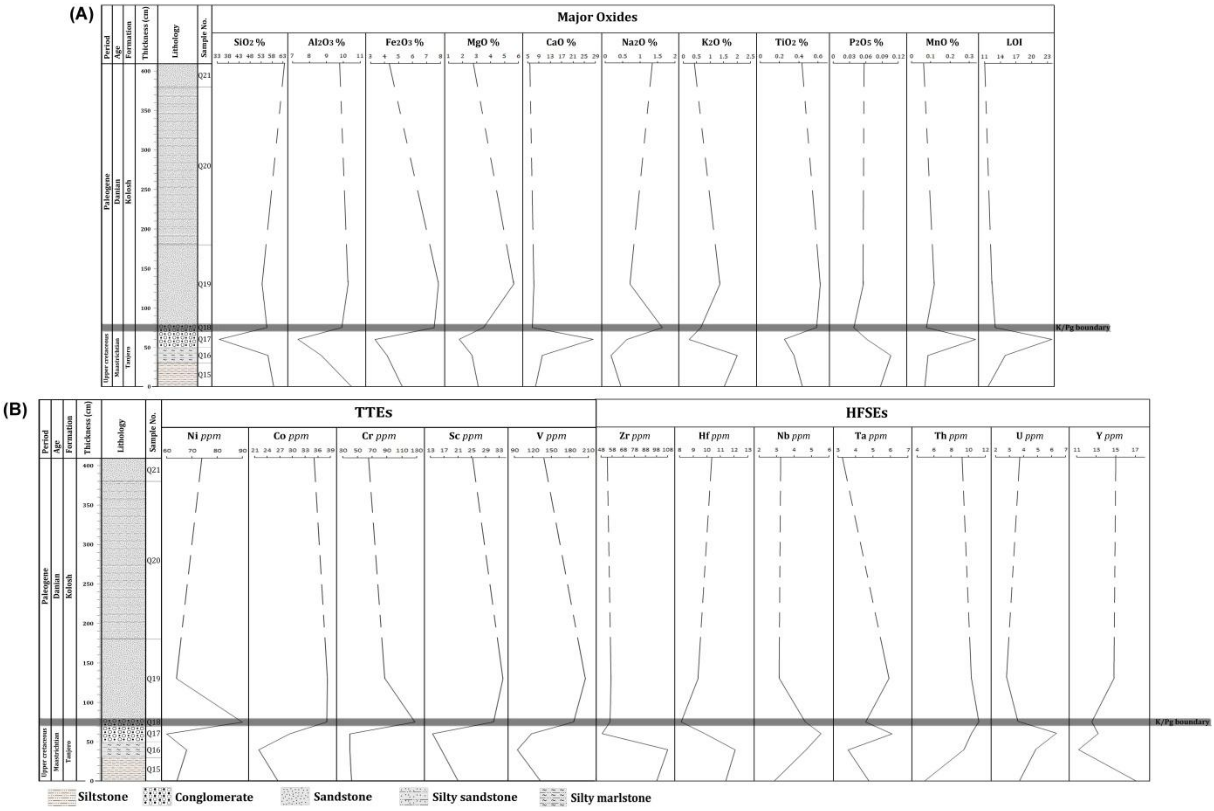

Fig. 20. Vertical distribution profile plot across the K/Pg boundary from the Qalbaza section. (A) Major oxides with LOI. (B) Transition trace elements (TTEs) and high field strength elements (HFSEs). Sample Q20 was not analyzed; the gray area represents the K/Pg boundary layer.

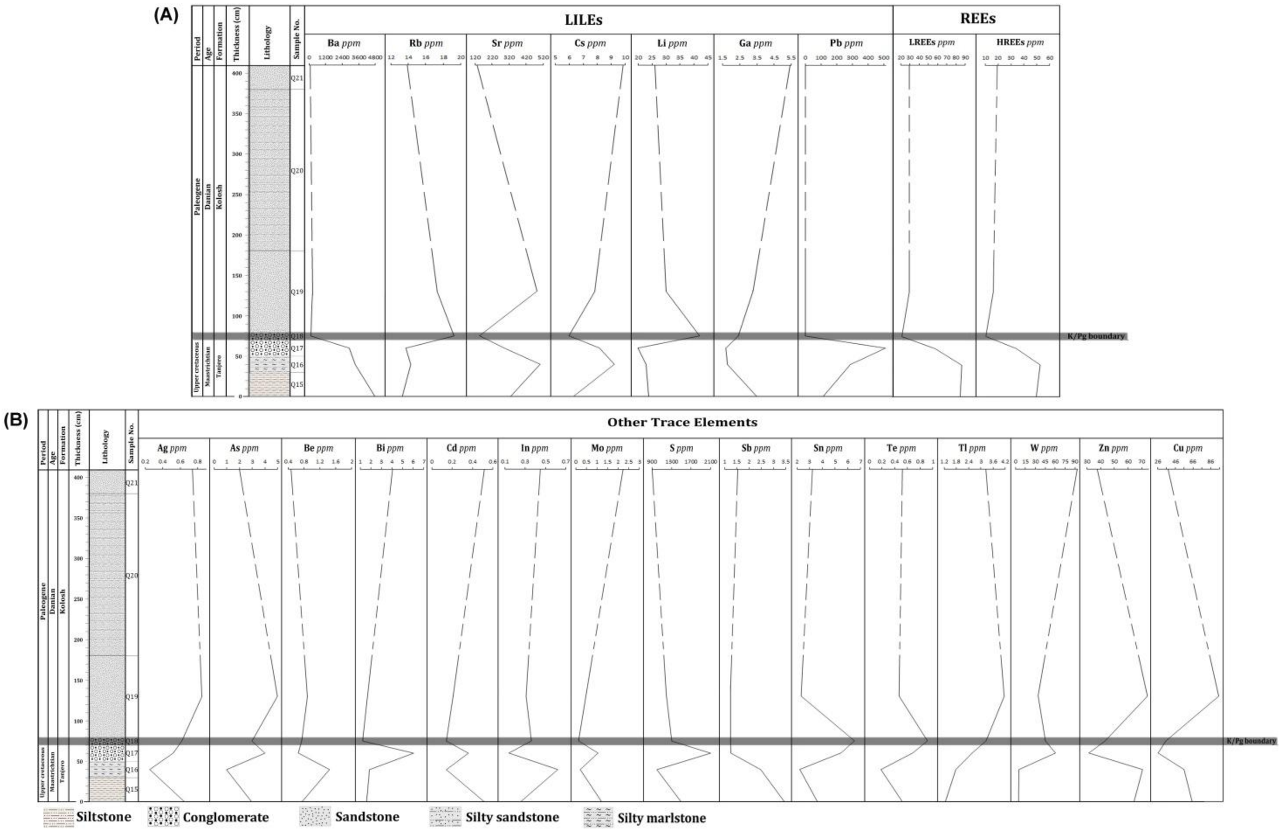

Fig. 21. Vertical distribution profile plot across the K/Pg boundary from the Qalbaza section. (A) Large ion lithophile elements (LILEs), light rare earth elements (LREEs), and heavy rare earth elements (HREEs) (B) Ag, As, Be, Bi, Cd, In, Mo, S, Sb, Sn, Te, Tl, W, Zn, and Cu elements. Sample Q20 was not analyzed; the gray area represents the K/Pg boundary layer.

Table 13: Element/Al and SO_2/MnO ratios in the studied samples across the K/Pg boundary from Gali and Qalbaza sections.

Section	Sample	Fe/Al	Ni/Al	Cr/Al	SO_2/MnO
Gali	G22	1.097	0.0154	0.0090	0.537
	G21	1.291	0.0167	0.0067	0.563
	G20	1.055	0.0108	0.0037	0.164
	G19 (K/Pg)	1.522	0.0155	0.0077	1.042
	G18	1.462	0.0130	0.0041	0.925
Qalbaza	Q21	0.586	0.0014	0.0013	9.350
	Q19	1.007	0.0012	0.0016	6.901
	Q18 (K/Pg)	1.009	0.0017	0.0024	9.791
	Q17	0.577	0.0015	0.0010	4.169
	Q16	0.660	0.0015	0.0009	5.670
	Q15	0.663	0.0012	0.0008	11.094

Moreover, a sharp reduction in CaO may be attributed to acidic rain caused by Chicxulub and/or Deccan events, which temporarily prevented the development of $CaCO_3$ during the K/Pg boundary event (Keller et al., 2011). LOI shows a strong positive correlation with CaO in the studied sections (r = 0.99 for Gali and Qalbaza sections, respectively), indicating a drop in LOI at K/Pg boundaries of the current study. The reasons behind the depletion of trace elements at low temperatures are not well understood. Depletion mechanisms are influenced by trace element solubility, oxygen fugacity, and pH in aqueous environments (Ritter et al., 2015). Consequently, we are simply describing the possibility of detecting the K/Pg boundary.

According to geochemical results, the G19 and Q18 layers of the Gali and Qalbaza sections, respectively, appear to have originated during the Cretaceous and Paleogene periods.

Conclusion

The main conclusions of this study are:

1. Gali and Qalbaza sandstones are immature lithic graywacke derived from the undissected arc-recycled orogenic provenance and deposited in an arid to semi-arid paleoclimate.
2. Vermiculite, smectite, and analcime phases support arid-semi-arid paleoclimate conditions for Gali and Qalbaza sediments.
3. Rare earth elements (REE) suggested a single melt suffered differentiation to provide the source rocks that weathered and deposited under oxic-anoxic paleoredox conditions.
4. Carbonate rock fragments, chert, and heavy minerals decreased, while total quartz and K-feldspar increased by 10 cm thick in both the grey siltstone of the Gali section and the red conglomerate of the Qalbaza section.
5. At 10 cm thick, low calcite content, high quartz content, analcime, smectite, and vermiculite have been identified in both the grey siltstone of the Gali section and the red conglomerate of the Qalbaza section.
6. Positive anomalies for SiO_2, Al_2O_3, Fe_2O_3, MgO, Na_2O, K_2O, TTEs, Zr, Zn, and Cu, and negative anomalies for CaO, MnO, LOI, Hf, Sr, and Cs were recorded at 10 cm thick in both the grey siltstone of the Gali section and red conglomerate of Qalbaza section.
7. Elevated levels of Fe/Al, Ni/Al, Cr/Al, and SO_2/MnO were detected at 10 cm thick of gray siltstone and red conglomerate layers from the Gali and Qalbaza sections, respectively.
8. Based on the current mineralogical and geochemical evidence, the proposed boundaries of gray siltstone and red conglomerate layers from the Gali and Qalbaza sections, respectively, could represent the K/Pg boundaries, with parts of them perhaps eroded.

Acknowledgements

We are grateful to the Department of Geology at Basrah University for the facilities they provide. We would also like to thank Dr. Kamal Karim, Dr. Nabaz Aziz, Mr. Madyan

Al-Gburi, and Mr. Irfan Asaad for their assistance in the fieldwork and sampling. We are very thankful to Dr. Kotayba Al-Youzbakey, Dr. Ahid Almallah, Dr. Zaid Malak, Dr. Safwan Al-Lhaebi, and Dr. Salem Hamed for their valuable discussions that supported this study. We also thank the Journal's Editor in Chief, Secretary, Technical Editors, and Reviewers for their valuable contributions and suggestions.

References

Abawi, T.S., Abdel Kireem, M.R. and Yousef, G.M., 1982. Planktonic foraminiferal stratigraphy of the Shiranish Formation, Sulaimaniah-Dokan region Northeastern Iraq, Revista Espanola de Micropaleontologia, Vol. 14, No. 1-3, pp. 153-164. https://dialnet.unirioja.es/servlet/articulo?codigo=8997713.

Adatte, T., Keller, G., Burns, S., Stoykova, K.H., Ivanov, M.I., Vangelov, D., Kramar, U. and Stuben, D., 2002. Paleoenvironment across the Cretaceous-Tertiary transition in eastern Bulgaria, in Adatte, T., Koeberl, C., and MacLeod, K.G., eds., Catastrophic Events and Mass Extinctions: Impacts and Beyond: Boulder, Colorado, Geological Society of America Special Paper 356, pp. 231–251. DOI: 10.1130/0-8137-2356-6.231.

Al-Hamed, S.T. and Malak, Z.A., 2021. Comparison Between the Classical Classification and Digital Classification for Selected Samples of Igneous and Carbonate Rocks. Iraqi Geological Journal, Vol. 54, No. 1C, pp. 16-29. Doi: 10.46717/igj.54.1C.2Ms-2021-03-22.

Al-Hamidi, R.I., Al-Hamed, S.T., Malak, Z.A. and Al-Sanjary, A.A., 2023. Mineralogy and Geochemistry of Sandstones from the Tanjero Formation, Bekhme Gorge Northeastern Iraq: Implications for Paleoweathering and Provenance. The Iraqi Geological Journal, Vol. 56, No. 1C, pp. 25-39. DOI: 10.46717/igj.56.1C.3ms-2023-3-14.

Al-Qayim, B.A., Kharajiany, S.O.A. and Sherwood, W.W.Jr., 2020. Biostratigraphic analysis of the K/Pg boundary using calcareous nannofossils from the Sulaimani Area, Kurdistan Region, Iraq. Kuwait Jour.of Sci. and Eng., Vol. 47, No. 4, pp. 92-105.

Alvarez, L.W., Alvarez, W., Asaro, F. and Michel, H.V., 1980. Extraterrestrial cause for the Cretaceous-Tertiary extinction: Experimental results and theoretical interpretation. Science, Vol. 208, No. 4448, pp. 1095-1108. DOI: 10.1126/science.208.4448.1095.

Arakawa, Y., Li, X., Ebihara, M., Meriç, E., Tansel, I., Bargu, S. and Matsumaru, K., 2003. Element profiles and Ir concentration of Cretaceous-Tertiary (KT) boundary layers at Medetli, Gölpazari, northwestern Turkey. Geochemical journal, Vol. 37, No. 6, pp. 681-693. DOI: 10.2343/geochemj.37.681.

Arenillas, I., Arz, J.A. and Molina, E., 2004. A new high-resolution planktonic foraminiferal zonation and subzonation for the lower Danian. Lethaia, Vol. 37, No. 1, pp. 79–95. DOI: 10.1080/00241160310005097.

Bardeen, C.G., Garcia, R.R., Toon, O.B. and Conley, A.J., 2017. On transient climate change at the Cretaceous-Paleogene boundary due to atmospheric soot injections. Proceedings of the National Academy of Sciences USA, Vol. 114, No. 36, pp. E7415–E7424. DOI: 10.1073/pnas.1708980114.

Bercovici, A., Vajda, V., Pearson, D., Villanueva-Amadoz, U. and Kline, D., 2012. Palynostratigraphy of John's Nose, a new Cretaceous–Paleogene boundary section in southwestern North Dakota, USA. Palynology, Vol. 36, No. 1, pp. 36-47. DOI: 10.1080/01916122.2012.678695.

Boggs, S.J., 2006. Principles of sedimentology and stratigraphy. 4th ed., Pearson Prentice Hall, Upper Saddle River, New Jersey, 662 p. Online version: 647640269.

Bourgeois, J., Hansen, T.A., Wiberg, P.L. and Kauffman, E.G., 1988. A Tsunami Deposit at the Cretaceous-Tertiary Boundary in Texas. Science, Vol. 241, No.4865, pp. 567–570. DOI: 10.1126/science.241.4865.567.

Brookins, D.G., 1989. Aqueous geochemistry of rare earth elements. In: Lipin BR, McKay GAŽ (eds) Geochemistry and mineralogy of rare earth elements. Reviews in Mineralogy and Geochemistry, Vol. 21, No. 1, pp. 201-225.

Buday, T. and Jassim, S., 1987. The Regional Geology of Iraq: Tectonics, Magmatism, and Metamorphism. In: Kassab, I.I. and Abbas, M.J., Eds, Stratigraphy, State Establishment of Geological Survey and Mineral Investigations, Baghdad, pp. 1-445.

Buday, T. and Jassim, S.Z., 1984. Tectonic Map of Iraq, Scale 1:1,000,000. GEOSURV, Baghdad. https://www.scirp.org/reference/referencespapers?referenceid=1264156.

Carroll, D.C., 1970. Clay minerals: A guide to their X-Ray identification. The Geological Society of America, Special Paper 126, Colorado Building, 80 p.

Carver, R.E., 1971. Procedures in sedimentary petrology. John Wiley and Sons, New York, 653 P.

Çelik, H. and Salih, H.M.H., 2021. Petrographic characteristics of deep marine turbidite sandstones of the Upper Cretaceous Tanjero Formation, Northwestern Sulaimaniyah, Iraq: implications for provenance and tectonic setting. Bulletin of the Mineral Research and Exploration, Vol. 164, No. 164, pp. 11-38. DOI: 10.19111/bulletinofmre.800132.

Coccioni, R. and Premoli Silva, I., 2015. Revised Upper Albian – Maastrichtian planktonic foraminiferal biostratigraphy and magnetostratigraphy of the classical Tethyan Gubbio section (Italy). Newsletters on Stratigraphy, Vol. 48, No. 1, pp. 47-90. DOI: 10.1127/nos/2015/0055.

Coombs, D.S., 1954. The nature and alteration of some Triassic sediments from Southland, New Zealand. In Transactions of the Royal Society of New Zealand, Vol. 82, No. 65, 109 p.

De Baar, H.J., Bacon, M.P., Brewer, P.G. and Bruland, K.W., 1985. Rare earth elements in the Pacific and Atlantic Oceans. Geochimica et Cosmochimica Acta, Vol. 49, No. 9, pp. 1943-1959. DOI: 10.1016/0016-7037(85)90089-4.

Dickinson, W.R. and Suczek, C.A., 1979. Plate tectonics and sandstone compositions. Aapg Bulletin, Vol. 63, No. 12, pp. 2164-2182. DOI: 10.1306/2F9188FB-16CE-11D7-8645000102C1865D.

Dickinson, W.R., 1985. Interpreting Provenance Relations from Detrital Modes of Sandstones. In: Zuffa, G.G. (eds) Provenance of Arenites. NATO ASI Series, Springer, Dordrecht, vol 148, pp. 333 -361. DOI: 10.1007/978-94-017-2809-6_15.

Dott, R.H., 1964. Wacke, greywacke and matrix; what approach to immature sandstone classification. Journal of Sedimentary Research, Vol. 34, No. 3, pp. 625-632. DOI: 10.1306/74D71109-2B21-11D7-8648000102C1865D.

Dunham, R.J., 1962. Classification of carbonate rocks according to depositional textures. In: Classification of Carbonate Rocks — A Symposium, ed. By Ham, William E. AAPG Memoir, 1. AAPG (American Association of Petroleum Geologists), Tulsa, Oklahoma, pp. 108-121. ISBN: 9781629812366.

Font, E., Adatte, T., Andrade, M., Keller, G., Bitchong, A.M., Carvallo, C., Ferreira, J., Diogo, Z. and Mirão, J., 2018. Deccan volcanism induced high-stress environment during the Cretaceous–Paleogene transition at Zumaia, Spain: Evidence from magnetic, mineralogical and biostratigraphic records. Earth and Planetary Science Letters, 484, pp. 53-66. DOI: 10.1016/j.epsl.2017.11.055.

Gilmour, I. and Anders, E., 1989. Cretaceous-Tertiary boundary event: Evidence for a short time scale. Geochimica et Cosmochimica Acta, Vol. 53, No. 2, pp. 503-511. DOI: 10.1016/0016-7037(89)90401-8.

Graup, G. and Spettel, B., 1989. Mineralogy and phase-chemistry of an Ir-enriched pre-K/T layer from the Lattengebirge, Bavarian Alps, and significance for the KTB problem. Earth and Planetary Science Letters, Vol. 95, No. 3-4, pp. 271-290. DOI: 10.1016/0012-821X(89)90102-7.

Gribble, C.D., Hall, A.J., 1985. The non-silicates. In: A Practical Introduction to Optical Mineralogy. Springer, Dordrecht, pp. 132-172.

Harder, H., 1972. The role of magnesium in the formation of smectite minerals. Chemical Geology, Vol. 10, No. 1, pp. 31-39. DOI: 10.1016/0009-2541(72)90075-7.

Horton, D.G., 1985. Mixed-layer illite/smectite as a paleotemperature indicator in the Amethyst vein system, Creede district, Colorado, USA. Contributions to Mineralogy and Petrology, Vol. 91, No. 2, pp. 171-179. DOI: 10.1007/BF00377764.

Iijima, A. and Utada, M., 1966. Zeolites in sedimentary rocks, with reference to the depositional environments and zonal distribution. Wiley, Vol. 7. No. 4. pp. 327-357.

Ingersoll, R.V. and Suczek, C.A., 1979. Petrology and provenance of Neogene sand from Nicobar and Bengal fans, DSDP sites 211 and 218. Jour. of Sedimentary Research, Vol. 49, No. 4, pp. 1217-1228. DOI: 10.1306/212F78F1-2B24-11D7-8648000102C1865D.

Jassim, S.Z. and Buday, T., 2006. Tectonic framework. In: S.Z. Jassim and J.C. Goff (eds), Geology of Iraq. Publication of Dolin, Prague and Moravian Museum, Brno, 341 P.

Joanna M., Cristiano L., Anton K., Barry C., Claire B., Sandro M., Enrique D.M., Antonio B., and Virginio N., 2006. Analyses of shocked quartz at the global K-P boundary indicate an origin from a single, high-angle, oblique impact at Chicxulub, Earth and Planetary Science Letters, Vol. 251, No. 3-4, pp. 264-279. DOI: 10.1016/j.epsl.2006.09.009.

Jorge L. Cobiella, R., Esther M.C.G., Silvia B.B., Lourdes P.E, Santa G.G. and Yania P.R., 2015. Cretaceous-Paleogene boundary deposits and paleogeography in western and central Cuba. Revista Mexicana de Ciencias Geológicas, Vol. 32, No. 1, pp. 156-176.

Karim, K.H., 2004. Basin analysis of Tanjero Formation in Sulaimaniya area, NE-Iraq. Unpublished Ph.D. thesis, University of Sulaimani, 135 P.

Keller, G., 2014. Deccan volcanism, the Chicxulub impact, and the end-Cretaceous mass extinction: Coincidence? Cause and effect. Geological Society of America Special Papers, 505, pp. 57-89. DOI: 10.1130/2014.2505(03).

Keller, G., Adatte, T., Bhowmick, P.K., Upadhyay, H., Dave, A., Reddy, A.N. and Jaiprakash, B.C., 2012. Nature and timing of extinctions in Cretaceous-Tertiary planktic foraminifera preserved in Deccan intertrappean sediments of the Krishna-Godavari Basin, India, Earth and Planetary Science Letters, Vol. 341–344, pp. 211-221. DOI:10.1016/j.epsl.2012.06.021.

Keller, G., Bhowmick, P.K., Upadhyay, H., Dave, A., Reddy, A.N., Jaiprakash, B.C. and Adatte, T., 2011. Deccan volcanism linked to the Cretaceous-Tertiary boundary (KTB) mass extinction. New evidence from ONGC wells in the Krishna-Godavari Basin, India:

Journal of the Geological Society of India, Vol. 78, pp. 399-428. DOI:10.1007/s12594-011-0107-3.

Kring, D.A., Tikoo, S.M., Schmieder, M., Riller, U., Rebolledo-Vieyra, M., Simpson, S.L. and Yamaguchi, K.E., 2020. Probing the hydrothermal system of the Chicxulub impact crater. Science Advances, Vol. 6, No. 22, eaaz3053. DOI: 10.1126/sciadv.aaz3053.

Liou, J.G., de Capitani, C. and Frey, M., 1991. Zeolite equilibria in the system $CaAI_2Si_2O_8$-$NaAISi_3O_8$-SiO_2-H_2O. New Zealand Journal of Geology and Geophysics, Vol. 34, No. 3, pp. 293-301. DOI: 10.1080/00288306.1991.9514467.

Mateo P., Keller, G., Adatte, T., Bitchong, A.M., Spangenberg, J.E., Vennemann, T. and Hollis, J.C., 2019. Deposition and age of Chicxulub impact spherules on Gorgonilla Island, Colombia. Geological Society of America. GSA Bulletin. V. 132, No. 1-2, pp. 215-232. DOI. 10.1130/B35287.1.

Montano, D., Gasparrini, M., Rohais, S. and De Luca, R., 2023. A Lacustrine Record for the Cretaceous–Paleogene Boundary-Yacoraite Fm., (Northwest Argentina). Geosciences. Vol. 13, No. 8, 227 P. DOI: 10.3390/geosciences13080227.

Nichols, G., 2009. Sedimentary and stratigraphy, Blackwell Publishing Company, UK, 355 P. ISBN 978-1-4051-3592-4.

Nwajide, C.S. and Hoque, M., 1985. Problem of classification and maturity evaluation of a diagnostically altered fluvial sandstone. Geologic en mijnb., Vol.64, No. 1, pp. 69-77.

Petersen, S. V., Dutton, A. and Lohmann, K.C., 2016. End-Cretaceous extinction in Antarctica linked to both Deccan volcanism and meteorite impact via climate change. Nature. Communications Vol. 7, 12079 P. DOI: 10.1038/ncomms12079.

Pettijohn, F.J., 1975. Sedimentary Rocks. 3rd Edition, Harper and Row, New York, 628 P.

Pitakpaivan, K., Byerly, G.R. and Hazel, J.E., 1994. Pseudomorphs of impact spherules from a Cretaceous-Tertiary boundary section at Shell Creek, Alabama. Earth and planetary science letters, Vol. 124, No. 1-4, pp. 49-56. DOI: 10.1016/0012-821X(94)00077-8.

Potter, P.E. and Pettijohn, F.J., 1977. Paleocurrent and Basin Analysis, 2nd Edition, Springer-Verlag Berlin, 425 P.

Premović, P.I., 2004. Cretaceous-Tertiary boundary deposits in Denmark: A diachroneity. Journal of the Serbian Chemical Society, Vol. 69, No. 7, pp. 555-561. DOI: 10.2298/JSC0407555P.

Prinn, R.G. and Fegley Jr, B., 1987. Bolide impacts, acid rain, and biospheric traumas at the Cretaceous-Tertiary boundary. Earth and Planetary Science Letters, Vol. 83, No. 1-4, pp. 1-15. DOI: 10.1016/0012-821X(87)90046-X.

Renne, P.R., Sprain, C.J., Richards, M.A., Self, S., Vanderkluysen, L. and Pande, K., 2015. State shift in Deccan volcanism at the Cretaceous-Paleogene boundary, possibly induced by impact, Science, Vol. 350, No. 6256, pp. 76-78. DOI: 10.1126/science.aac754.

Ritter, X., Deutsch, A., Berndt, J. and Robin, E., 2015. Impact glass spherules in the Chicxulub K-Pg event bed at Beloc, Haiti: Alteration patterns. Meteoritics and Planetary Science, Vol. 50, No. 3, pp. 418-432. DOI: 10.1111/maps.12432.

Sharbazheri, K.M., 2008. Biostratigraphy and Paleoecology of Cretaceous/Tertiary Boundary in The Sulaimani Region, Kurdistan, NE-Iraq. Unpublished Ph.D. Thesis, University of Sulaimani, Iraq, 219 p.

Sholkovitz, S.R., Landing, W.M. and Lewis, B.L., 1994. Ocean Particle Chemistry: The fractionation of rare earth elements between suspended particles and seawater. Geochimica et Cosmochimica Acta, Vol. 58, No. 6, 1994, pp. 1567-1579. DOI: 10.1016/0016-7037(94)90559-2.

Sial, A.N., Chen, J., Lacerda, L.D., Frei, R., Higgins, J.A., Tewari, V.C., Gaucher, C., Ferreira, V.P., Cirilli, S., Korte, C., Barbosa, J.A., Pereira, N.S. and Ramos, D.S., 2019. Chemostratigraphy Across the Cretaceous-Paleogene (K-Pg) Boundary: Testing the Impact and Volcanism Hypotheses, American Geophysical Union, John Wiley & Sons, Inc. Chapter 12, Edited by Alcides N. Sial, Claudio Gaucher, Muthuvairavasamy Ramkumar, and Valderez Pinto Ferreira, pp. 223-258. DOI: 10.1002/9781119382508.

Sissakian, V.K. and Fouad, S.F., 2015. Geological map of Iraq, scale 1: 1000 000, 2012. Iraqi Bulletin of Geology and Mining, Vol. 11, No. 1, pp. 9-16.

Smit, J., 1982. Extinction and evolution of planktonic foraminifera after a major impact at the Cretaceous/Tertiary boundary, Geological Implications of Impacts of Large Asteroids and Comets on the Earth, Leon T. Silver, Peter H. Schultz, pp. 329–352. DOI: 10.1130/SPE190-p329.

Smit, J., 1999. The global stratigraphy of the Cretaceous-Tertiary boundary impact ejecta. Annual Review of Earth and Planetary Sciences, Vol. 27, No. 1, pp. 75-113. DOI: 10.1146/annurev.earth.27.1.75.

Smit, J. and ten Kate, W.G.H.Z., 1982. Trace-element patterns at the Cretaceous-Tertiary boundary—consequences of a large impact. Cretaceous research, Vol. 3, No. 3, pp. 307-332. DOI: 10.1016/0195-6671(82)90031-3.

Sosa-Montes De Oca, C, De Lange, G.J., Martínez-Ruiz, F., Ortega-Huertas, M. and Rodríguez-Tovar, F.J., 2020. Microscale trace-element distribution across the Cretaceous/Palaeogene ejecta layer at the Agost section: Constraining the recovery of pre-impact conditions. *Chemical Geology*, *533*, 119431, 10 P. DOI: 10.1016/j.chemgeo.2019.119431.

Sosa-Montes De Oca, C., Martínez-Ruiz, F. and Rodríguez-Tovar, F.J., 2013. Bottom-water conditions in a marine basin after the Cretaceous–Paleogene impact event: timing the recovery of oxygen levels and productivity. PLoS One, Vol. 8, No. 12, 7 P. DOI: 10.1371/journal.pone.0082242.

Sun, S.S. and McDonough, W.F., 1989. Chemical and isotopic systematics of oceanic basalts: implications for mantle composition and processes. Geological Society, London, Special Publications, Vol. 42, No. 1, pp. 313-345. DOI: 10.1144/GSL.SP.1989.042.01.19.

Suttner, L.J. and Dutta, P.K., 1986. Alluvial sandstone composition and paleoclimate; I, Framework Mineralogy. Journal Sedimentary Research, Vol. 56, No. 3, pp. 329-345. DOI: 10.1306/212F8909-2B24-11D7-8648000102C1865D.

Taylor, S.R. and McLennan, S.M., 1985. The Continental Crust: Its Composition and Evolution. Blackwell, Scientific Publication, Oxford. 312 P. DOI: 10.1002/gj.3350210116.

Trubelja, F., Marchig, V., Burgath, K.P. and Vujović, Ž., 1995. Origin of the Jurassic Tethyan ophiolites in Bosnia: a geochemical approach to tectonic setting. Geologia Croatica, Vol. 48, No. 1, pp. 49-66. https://hrcak.srce.hr/18012.

Vajda, V. and Wigforss-Lange, J., 2006. The Jurassic-Cretaceous transition of Southern Sweden–Palynological and sedimentological interpretation. Progress in Natural Science, Vol. 16, No. 1, pp. 31-38. DOI: 10.1080/10020070612330073A.

Zattin, M. and Zuffa, G.G., 2004. Unravelling the source rocks of Late Eocene-Miocene orogenic wedge and foredeep arenites of the northern Apennines and southern Alps. Bollettino Della Societa Geologica Italiana, Vol. 123, No.1, pp. 67-76. https://api.semanticscholar.org/CorpusID:131986124.